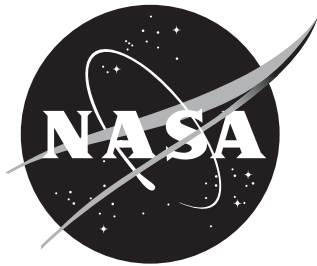


NASA/TM-2014-218353



**On Parametric Sensitivity of
Reynolds-Averaged Navier-Stokes SST Turbulence Model:
2D Hypersonic Shock-Wave Boundary-Layer Interactions**

*James L. Brown, Ph.D.
NASA Ames Research Center, Moffett Field, CA*

May 2014

NASA STI Program . . . in Profile

Since its founding, NASA has been dedicated to the advancement of aeronautics and space science. The NASA scientific and technical information (STI) program plays a key part in helping NASA maintain this important role.

The NASA STI Program operates under the auspices of the Agency Chief Information Officer. It collects, organizes, provides for archiving, and disseminates NASA's STI. The NASA STI Program provides access to the NASA Aeronautics and Space Database and its public interface, the NASA Technical Report Server, thus providing one of the largest collection of aeronautical and space science STI in the world. Results are published in both non-NASA channels and by NASA in the NASA STI Report Series, which includes the following report types:

- **TECHNICAL PUBLICATION.**
Reports of completed research or a major significant phase of research that present the results of NASA programs and include extensive data or theoretical analysis. Includes compilations of significant scientific and technical data and information deemed to be of continuing reference value. NASA counterpart of peer-reviewed formal professional papers, but having less stringent limitations on manuscript length and extent of graphic presentations.
- **TECHNICAL MEMORANDUM.**
Scientific and technical findings that are preliminary or of specialized interest, e.g., quick release reports, working papers, and bibliographies that contain minimal annotation. Does not contain extensive analysis.
- **CONTRACTOR REPORT.**
Scientific and technical findings by NASA-sponsored contractors and grantees.

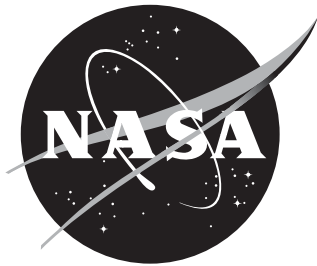
- **CONFERENCE PUBLICATION.**
Collected papers from scientific and technical conferences, symposia, seminars, or other meetings sponsored or co-sponsored by NASA.
- **SPECIAL PUBLICATION.**
Scientific, technical, or historical information from NASA programs, projects, and missions, often concerned with subjects having substantial public interest.
- **TECHNICAL TRANSLATION.**
English- language translations of foreign scientific and technical material pertinent to NASA's mission.

Specialized services also include creating custom thesauri, building customized databases, and organizing and publishing research results.

For more information about the NASA STI Program, see the following:

- Access the NASA STI program home page at <http://www.sti.nasa.gov>
- E-mail your question via the Internet to help@sti.nasa.gov
- Fax your question to the NASA STI Help Desk at 443-757-5803
- Phone the NASA STI Help Desk at 443-757-5802
- Write to:
NASA STI Help Desk
NASA Center for Aerospace
Information
7115 Standard Drive
Hanover, MD 21076-1320

NASA/TM-2014-218353



**On Parametric Sensitivity of
Reynolds-Averaged Navier-Stokes SST Turbulence Model:
2D Hypersonic Shock-Wave Boundary-Layer Interactions**

*James L. Brown, Ph.D.
NASA Ames Research Center, Moffett Field, CA*

National Aeronautics and
Space Administration

Ames Research Center
Moffett Field, CA 94035-1000

May 2014

Acknowledgments

This work was sponsored by NASA's Hypersonic Entry Descent and Landing (HEDL/STMD) projects.

The author gratefully acknowledges discussions with Joseph G. Marvin on free interaction theory.

The use of trademarks or names of manufacturers in this report is for accurate reporting and does not constitute an official endorsement, either expressed or implied, of such products or manufacturers by the National Aeronautics and Space Administration.

Available from:

NASA Center for AeroSpace Information
7115 Standard Drive
Hanover, MD 21076-1320
443-757-5802

Abstract

Examined is sensitivity of separation extent, wall pressure and heating to variation of primary input flow parameters, such as Mach and Reynolds numbers and shock strength, for 2D and Axisymmetric Hypersonic Shock Wave Turbulent Boundary Layer interactions obtained by Navier-Stokes methods using the SST turbulence model. Baseline parametric sensitivity response is provided in part by comparison with vetted experiments, and in part through updated correlations based on free interaction theory concepts. A recent database compilation of hypersonic 2D shock-wave/turbulent boundary layer experiments extensively used in a prior related uncertainty analysis provides the foundation for this updated correlation approach, as well as for more conventional validation. The primary CFD method for this work is DPLR, one of NASA's real-gas aerothermodynamic production RANS codes. Comparisons are also made with CFL3D, one of NASA's mature perfect-gas RANS codes. Deficiencies in predicted separation response of RANS/SST solutions to parametric variations of test conditions are summarized, along with recommendations as to future turbulence approach.

1 Introduction

Design optimization for aerodynamic and aeroheating of hypersonic and reentry vehicles rely on advanced computational methods, such as RANS (Reynolds-Averaged Navier-Stokes) CFD codes with advanced turbulence models, validated for correct response over a sufficient range for input relevant design parameters. Conventionally, this validation is done by comparison of CFD results with a select group of experiments at discrete fluid dynamic conditions. However, credibility of optimization results rely not just on conventional CFD validation for discrete experimental conditions at sparse points located in parameter space, but also by ensuring the proper response trends of the underlying analysis procedures throughout the entire input parameter space considered.

Multi-Discipline Optimization (MDO) procedures, embedded with RANS methods and reliance on advanced turbulence models, when applied to the design of modern Hypersonic and Atmospheric ReEntry vehicles (Garcia, et al., [1]) can result in aerothermodynamic performance gains combined with weight savings so as to exhibit potential for improved mission operations and costs with consequent enhanced economic viability of the evolving nascent US Space industry. The success of these MDO Optimization procedures depends not just on their algorithmic efficiency, but also on the physical accuracy of the modeling of the turbulent RANS analysis procedures over a large range of possible vehicle and fluid dynamic performance parameters. The validation of turbulent models in RANS procedures, however, often depends on com-

parisons of turbulent RANS analysis results with but a small number of vetted available experiments covering only a small range of physical parameters.

Examination of the sensitivity of these turbulent RANS analysis methods to fluid dynamic parametric variations relative to established correlations in conjunction to these vetted experiments help establish the degree and range of credibility for optimized design results of MDO procedures with embedded turbulent RANS aerothermodynamic analysis. One such recent uncertainty analysis was accomplished by the present author (Brown, Refs. [2,3]) at the discrete conditions of a vetted database of hypersonic experiments (Marvin, Brown and Gnoffo, Ref. [4]. However, realized during the course of that study was that by considering only a limited number of fluid conditions as described by a small select group of experiments, no matter how well-behaved the experiments, leads to an incomplete picture of the analysis validity; rather, there is need to ensure that the proper physical trends are obeyed. Essentially, it is only when both the point-wise accuracy and the trend sensitivity of the turbulent RANS methods embedded in MDO methods are physically correct that optimized design results from MDO procedures can be trusted as being valid. By point-wise accuracy, we mean accuracy of design relevant quantities such as separation extent, separation bubble pressure, peak pressure and peak heating at the discrete flow parameters of the considered experiments, while by ‘trend sensitivity’ we mean the partial derivative or variation of these design relevant quantities with respect to small variations of the flow parameters (typically Mach number, Reynolds number, shock strength, wall cooling, etc.) about the discrete conditions of these considered experiments.

The present study attempts to examine the ability of current turbulent RANS methods applied to hypersonic Shock Wave Turbulent Boundary Layer Interactions by use of the recently released database of vetted hypersonic experiments (Marvin, et al., [4]), supplemented by the previous database of Settles and Dodson, Refs. [6]- [9]. Comparison of CFD results (such as separation extent, separation bubble pressure and peak heating) with such experiments provides a basis for credibility at the discrete fluid dynamic conditions of these experiments. But it does not provide confidence in the ability of these CFD methods to properly follow the correct trends (e.g., rate of change in {separation extent, separation bubble pressure or peak heating} with respect to incremental change in {Mach no, Reynolds number, wall cooling}) when the fluid dynamic conditions change over a large range as might be required to accomplish comprehensive MDO optimization. To accomplish examination of parametric trend sensitivity of these methods, we make use of correlations related to the long-established concept of free-interaction theory (Chapman, et al., [23], and Erdos and Pallone, [25]), updated, where needed, to include the latest hypersonic database. Other accepted correlations are to be considered as well. Only by identifying these deficiencies, can

an attempt then be made to advance CFD turbulence modeling so as to improve both the accuracy and the parametric trend sensitivity of the overall CFD turbulent analysis procedure.

A primary purpose of this paper is to evaluate and to identify deficiencies of current turbulent RANS CFD solution methods as applied to 2D Hypersonic Shock Wave Turbulent Boundary Layer Interactions, giving particular attention to the success of their results in conforming to proper trends with relevant fluid dynamic parametric variations.

In the following sections, we first provide a brief overview of two databases providing the hypersonic experimental data of primary use in this current report, next summarize the approach and results of the recent uncertainty analysis accomplished in the recent works of Brown [2,3] and of Gnoffo [19,20]. We then describe free interaction theory concepts and additional correlations that establish the proper physical parametric trends which computations should follow. The application of free interaction theory is reformulated slightly so as include and compare with these updated databases and also to better align the application of free interaction correlations to current CFD methodology. A comparison is then provided of turbulent CFD results with both the discrete experimental data of the databases and the parametric trends described by the updated free interaction related correlations. We finally identify defects in SST turbulence model response, so as to provide a basis for improved performance of the model relative to the database experiments and to free interaction theory. Primary emphasis is made of the Mach 8.2 Compression Corner experimental series of Holden and the Mach 2.85 Compression Corner experiments of Settles as these are two of but few hypersonic/supersonic datasets that includes variations in both shock strength and Reynolds number.

1.1 Hypersonic Shock-Wave Turbulent Boundary Layer Interaction Experiment Database

Much of the development of ‘Free Interaction’ SWBLI theory occurred based on early supersonic experiments. The primary source of experimental data used for the current study is obtained from two databases that include more recent hypersonic data and in a form that facilitates the use of that data. These are the supersonic/hypersonic database of Settles and Dodson [6], and the hypersonic database of Marvin, Brown and Gnoffo [4]. The databases themselves do not present new experimental data, but review the available experiments for the accuracy of the data, for complete definition of the geometry of the test and suitability and completeness of the stated test conditions for use with present-day Navier-Stokes solvers, and also seek permission from the experimenter to satisfy possible copyright issues. The databases then compile the data tabulated in easily read ASCII text files. More information can be obtained from the reports describing these databases, however the

experiments specifically used in this current study include both hypersonic and supersonic compression corner and impinging shock cases from Mach 3 to Mach 11, see Tables 1-4.

The primary parametric variation of interest to this study, that ideally would prove to be available in a single experiment having an upstream boundary layer of fixed properties, is a variation in shock strength from attached to incipient separation to several fully separated cases. Additional parameters of interest, likely to be found among the collection of experimental cases, and therefore having upstream boundary layers of differing properties, are variations in Reynolds number, Mach number and degree of wall cooling (T_w/T_{aw}). Of the experiments compiled in these two databases, the primary focus therefore will be on the Holden Mach 8 cold wall compression corner cases, the Settles Mach 3 adiabatic compression corner cases, and the Schülein Mach 5 cold wall impinging shock cases. The remaining experiments in these databases, as tabulated in Tables 1-4, then provide supplemental information to, at least partially, provide indication of the effects of Mach number, Reynolds number, degree of wall cooling and primary shock strength.

1.2 Computational Methods

Computational methods used for this study include both the EddyBL boundary layer code of Wilcox [13] to provide definition of the test flat plate (or axisymmetric cylinder) boundary layer, and DPLR, one of NASA's production Real-Gas Reynolds Averaged Navier-Stokes codes. The Wilcox 'EddyBL' boundary layer code with the Cebeci-Smith turbulence model option is used as the standard basis by which to evaluate the upstream flat plate boundary layer properties. However, it is the DPLR RANS code, using the SST turbulence model, and its' ability to properly analyze hypersonic shock wave turbulent boundary layer interaction behavior, that is of primary interest to this study. As all the experimental cases considered prove to be ideal gas, additional ideal-gas RANS solutions using the well-tested CFL3D code of Rumsey provide supplemental support to the DPLR/SST results.

These two codes, DPLR [14,15] and CFL3D [16], although providing the same nominal SST turbulence model of Menter [33]- [36], differ in details of the implementation of that viscous modeling, as well as their inviscid solver algorithm.

1.3 Uncertainty Analysis

NASA researchers provided, in a collection of papers, a recent uncertainty assessment of various aspects of hypersonic aerothermodynamics prediction capability, see Refs [17,18]. This included an assessment of two primary types of shock wave/turbulent boundary layer interactions: that of the compression corner, see Gnoffo [19,20]; and, of the

impinging shock wave boundary layer, see Brown [2, 3]. A goal of these last two papers was, based on rigorous statistical basis, to provide a confidence interval estimate of the performance of NASA production real-gas Navier-Stokes solvers in predicting selected design parameters (peak heating, peak pressure, separation extent, etc.) relevant to possible NASA mission and program needs for turbulent SWTBLI. This extended the conventional validation approach of simply examining and comparing, experiment by experiment, the performance of select turbulence models and CFD codes performance against each of the selected experiments, but also provided a collective CFD assessment over a range of conditions by statistical analysis of physics quantities of interest. The resultant uncertainty intervals should prove helpful in providing a rigorous statistical basis of risk assessment of NASA missions and programs interested in using CFD methods. Although an improvement over simple validation approaches used previously, one limitation is the small number of vetted experiments suitable for such a statistical analysis, but also that it only makes use of a *point* analysis from each experiment test condition, although collectively a wide range of test conditions are covered. What is not covered by such an approach is that about each experimental test condition (e.g. Mach number, Reynolds Number, Shock strength, etc), there exists a response in test results (separation extent, separation bubble pressure, peak wall pressure, peak wall heating, etc) covered by conventional validation, but also there exists a trend response of these same physical quantities of interest to small perturbations in test condition parameters, (e.g., $\partial \text{separation extent} / \partial \text{Mach Number}$, $\partial \text{separation extent} / \partial \text{Reynolds Number}$, etc). It is this latter ‘parametric trend response’ that we wish to explore more thoroughly, and to add to the validation process, in this present paper.

As to the Uncertainty Analysis conducted by both Gnoffo and by Brown, it was found that although separation extent and bubble pressure contributed to the overall uncertainty of current status of CFD solvers in prediction of SWTBLI, it is the post-reattachment wall heating that is the largest contributor to uncertainty, giving as much as $\approx 50\%$ overshoot. Such a large overshoot in wall heating prediction can have significant impact on NASA’s risk assessment in the design and operation of space vehicles, leading to unnecessarily large thermal protection systems, or limiting allowable mission performance. As such, there is a compelling need to reduce this uncertainty with improvements in CFD predictive methods, including advances in hypersonic turbulence models.

1.4 The ‘Free Interaction’ and λ -Shock Separation

A 2D or axisymmetric, supersonic or hypersonic boundary layer subjected to the sudden pressure rise of a primary shock system of sufficient strength will undergo separation. There are at least two distinct viscous-inviscid interactions that may be invoked for such a shock-separated re-

gion: the viscous-inviscid interaction controlling the separation process; and, the viscous-inviscid interaction controlling reattachment. It has been observed by experiment and by theoretical analysis, that the behavior of the separation region preceding the primary shock system is most directly defined by the properties of the boundary layer just upstream of separation regardless of the geometry of the primary shock system, whether by compression corner or by impinging shock, or forward facing step or obstacle or by means of a supersonic flow on the walls of an over expanded nozzle.

The overall shock-wave/boundary layer separation process is dominated by a strongly coupled viscous-inviscid interaction between the viscous separating boundary layer and the inviscid effects of the λ -shock that forms in response in the supersonic (or hypersonic) free stream immediately adjacent. The viscous and inviscid effects of this strong coupling are mutually induced. The separating boundary layer displacement thickness undergoes rapid growth induced by the inviscid pressure rise imposed on the boundary layer; the rapid displacement surface growth induces the formation of a leading λ -shock immediately above the separating boundary layer, and which projects upstream of the primary shock system. In turn, the λ -shock formation leads to a pressure rise imposed on the separating boundary layer. This shock-separation interaction has been found to be independent of, or free of primary dependence on, the details of the primary shock system; it has become known as a 'Free Interaction'. The λ -shock separation-for supersonic and hypersonic flows-process has proven to be nearly independent of the generating mode of the downstream primary shock system, whether that mode is of compression corner, of impinging shock, or of forward-facing step type. Rather, the properties of the 'Free Interaction' separation bubble (e.g. pressure level and shape of the pressure distribution within the separation bubble region) seem to be established by the properties of the upstream boundary layer: the primary controlling factors are observed to be the wall shear stress, wall pressure, boundary layer thickness (or displacement thickness), edge Mach number, and whether the boundary layer is turbulent or laminar.

In contrast, the process of reattachment of the separated boundary layer is subsequently accomplished in the vicinity of -and dependent on- the primary shock system, and not considered a 'Free Interaction'. Naturally, should the primary shock system not be of sufficient strength to separate the boundary layer, the primary shock system is still present, but without the leading λ -shock.

First order behavior observed characterizing 'Free Interaction' separation is that the shock angle of this leading λ shock and the magnitude of the associated pressure rise within the separation bubble, will remain nearly constant -once separation occurs- even if the strength of the primary shock system and its associated overall pressure rise is caused to increase. An increase in primary shock strength, past that needed to

separate the boundary layer, serves mainly to increase the extent or size of the separation bubble, but without significant further pressure rise within the separation region nor change in strength of the leading λ shock and its associated angle. It can be concluded that the ‘viscous-inviscid interaction’ of the leading λ shock with the underlying separating boundary layer is nearly independent -or ‘free’ of direct influence- of the primary shock system, and it is the ‘free interaction’ of the viscous separating boundary layer with the inviscid leading λ shock that establishes the properties of the separation bubble; consequently, the properties of the upstream boundary layer (e.g., the boundary layer wall shear stress, the boundary layer thickness, the edge Mach number, and whether the boundary layer is laminar, transitional or turbulent) that dominate in determining the details of the separation process and the properties of the leading λ shock.

1.4.1 Free Interaction Relations

Analyses of and relations describing the ‘Free Interaction’ were provided in experimental and theoretical studies predominantly in the mid-1950’s to early-1960’s. Extensions of the ‘Free Interaction’ concept to incorporate non-uniform free stream and real gas effects pertaining to rocket nozzle applications has occurred more recently. The paper of Chapman, Kuehn and Larson [23] appear to have first expressed the concept of ‘Free Interaction’ based on an analysis with integral boundary layer relations to convey the viscous effects and the Prandtl-Meyer relations to convey the inviscid effects, but with supporting dimensional analysis and extensive supersonic experimental observations. Chapman’s paper treated both turbulent and laminar cases, but limited to adiabatic wall boundary layers. A theoretical basis for ‘Free Interaction’ relations had been explored earlier by Reshotko and Tucker [24], but without clear identification of the ‘Free Interaction’ concept, and the latter thorough development by Erdos and Pallone [25] again using integral boundary layer and inviscid relations prevalent in that era. In each of these studies, a somewhat differing formulation was arrived at. Lewis, Kubota and Lees [26] improved the laminar case correlations to include cold-wall boundary layers. Carriere, Sirieix and Solignac [27] extended the cases considered to include turbulent separation in non-uniform supersonic flow. Additional experiments by Roshko and Thomke, by Settles, by Holden and others further enhanced the understanding of and credibility of ‘Free Interaction’ separation for supersonic and hypersonic shock-separated boundary layers.

Delery and Marvin [29] subsequently provided a comprehensive review, along with a summary of the primary behavior of the ‘Free Interaction’ to parametric variations. Apparent from Delery and Marvin’s review is that ‘Free Interaction’ theory certainly is not comprehensive in scope and should not be considered rigorous, as many effects are only

approximately inferred from theory, but appears to provide a robust framework to guide the formation of correlations of experimental data.

The form for the free interaction correlations used in this present study is that of the free interaction transformations describing the normalized pressure distribution, $\mathcal{P}_\xi(\xi)$ through the separation region as given in Equation 3.4 of Delery and Marvin, rearranged as:

$$\mathcal{P}_\xi(\xi) = (p_w(x) - p_{w,0})/\sqrt{2\tau_{w,0}q_0/\beta}, \text{ where} \quad (1)$$

$$\xi = (x - x_0)/\kappa_\xi\delta_0^*\sqrt{\beta\tau_{w,0}/q_0}, \text{ and} \quad (2)$$

$$(\ell_{sep}/\delta_0^*) = K(p_f - p_{f,incipient})/p_{w,0} \quad (3)$$

Where, the flow variables consisting of the skin friction, $\tau_{w,0}$, the dynamic pressure, $q_0 = \gamma p_{w,0} M_{e,0}^2/2$, and $\beta = \sqrt{(M_{e,0}^2 - 1)}$ appear in the relations above. Naturally, for air and N_2 , $\gamma = 1.4$.

The flow variables required for these transformations depend only on the upstream boundary layer, and so for a given upstream boundary layer, even where the primary shock strength varies with different experimental case, it is convenient to rewrite these equations as:

$$\mathcal{P}_\xi(\xi) = (p_w(x) - p_{w,0})/A_\xi, \quad (4)$$

$$\xi = (x - x_0)/\kappa_\xi B_\xi \delta_0^* \quad (5)$$

$$(\ell_{sep}/\delta_0^*) = K(p_f - p_{f,incipient})/p_{w,0} \quad (6)$$

Where, $A_\xi = \sqrt{2\tau_{w,0}q_0/\beta}$, and $B_\xi = 1/\sqrt{\beta\tau_{w,0}/q_0}$ are obtained using upstream boundary layer properties, and the variable κ_ξ is fit for each experiment of the wall pressure distribution through separation region to the standard curve of [25], but is constant for a particular upstream boundary layer regardless of whether primary shock strength is allowed to vary.

For turbulent flow:

$$\mathcal{P}_{\xi,s} = 4.22, \text{ at separation, } x_s, \text{ and} \quad (7)$$

$$\mathcal{P}_{\xi,b} = 6.0, \text{ for the separation bubble pressure plateau.} \quad (8)$$

Note, that the transformation required to obtain $\mathcal{P}_{\xi,s}$ and $\mathcal{P}_{\xi,b}$ levels does not require curve fit, but is determined entirely by the upstream boundary layer flow parameters, $\tau_{w,0}$, q_0 and β .

For this current study of the available hypersonic SWTBLI experiments, we make use of the Wilcox EddyBL boundary layer code using the Cebeci-Smith turbulent model to provide the upstream boundary properties for use in these relations (e.g., $\tau_{wall,0}$, etc.). Using the

EddyBL/Cebeci-Smith approach ensures consistent definition of the upstream boundary layer properties, and also casts these relations as providing a predictive method, rather than depending on the experimental measured boundary layer properties,

Note, that the growth of the separation bubble, as given by the separation length, ℓ , is seen to be linear with increase of p_f or ‘final’ pressure of the primary shock system over $p_{f,incipient}$ which is the ‘final’ pressure of the primary shock system for the case of incipient separation, as might be intuitively expected. The variable K is an experimental curve-fit, which may be dependent on Mach number, Reynolds number and degree of wall cooling.

ErDOS and Pallone did not provide a means of estimating the heat transfer behavior through the free interaction region, but other physics based discussions indicate that with onset of shock-separation, for the separation bubble region, the wall heating tends to initially decrease below upstream boundary layer values, even though the pressure rises, but then rises as reattachment is approached, and then follows the pressure-wall-heating correlation described below. However, no trend of wall heating variation in the separation region is clearly established in the various datasets to date, and so no free interaction theory for wall heating seems to have gained favor.

1.4.2 Free Interaction Trends

Whether based on free-interaction theory or simply on empirical observation, certain trends can be determined. Generally speaking as the Mach number increases, the turbulent boundary layer becomes more resistant to separation and it takes a larger induced pressure rise to initiate separation; and, as the Reynolds number increases (C_f decreases) then the turbulent boundary layer becomes less resistant to separation, leading to a lower induced pressure rise to initiate separation. Kuehn [28] based on extensive experimental data in the range of Mach 1.5-5, albeit mostly of axisymmetric flare, further states that the effect of heat transfer to the wall consistently reduces slightly the extent of separation; for axisymmetric cases a thin boundary layer relative to the cylinder diameter tends to promote separation; and, as might be expected, velocity profiles that were not fully developed as to turbulence were more prone to separation than fully developed boundary layers. The effect of bluntness of the flat plate or nose (entropy layer effect) on separation tended to be accounted for by using local properties, e.g. δ_0^* or C_f and M_e of the boundary layer just upstream of the interaction.

Whether such empirically observed trends are indeed correctly incorporated into current CFD methodology is, or should be a concern and is worthy of future analysis. There does seem to be a need for a comprehensive comparison of these and other semi-empirical correlations with a modern updated list of hypersonic experiments.

The physics based correlations stemming from free-interaction theory, as described in this subsection, provide a basis for behavior trends that will not be revealed by comparisons of CFD simulations with the few hypersonics experiment that exist. Also, as the free-interaction work was mainly accomplished based on supersonic experiments, there does seem to be a need for a comprehensive comparison of these and other semi-empirical correlations with a modern updated list of hypersonic experiments. What may be reasonably inferred from the CFD RANS hypersonic shock-separated flow simulation results that follow in the present study is that *the understanding reflected in the extensive experimental correlations related to free interaction theory has not been infused into standard available turbulence models*. It is this deficiency in existing turbulence models that may be a core reason for the high level of statistical variance and uncertainty that is exhibited by CFD simulations of hypersonic SWTBLI flows.

1.5 SWTBLI Pressure-Heating Correlations

A correlation of the variation of wall heating with wall pressure for SWTBL interactions was reported by Back and Cuffel [30], and further demonstrated by others, e.g. Holden [31], mainly that throughout the attached region of a SWTBL interaction-but not within a separation bubble, if it exists- the heating scales with pressure variation approximately as:

$$Q_{P85} \equiv Q_0 \cdot (p/p_0)^{0.85}, \quad \text{for turbulent 2D SWTBLI} \quad (9)$$

As with the separated region free-interaction relations (for pressure), the pressure-heating correlation appears to correlate a great deal of experimental data regardless of whether the interaction itself is of the compression corner or impinging shock type.

In that current RANS methods have difficulty predicting wall heating in the vicinity of reattachment of shock-separated flows, a more accurate approach for heating analysis of separated SWTBLI may be to post-analyze the CFD simulation pressure rise in the post-reattachment region using this $Q \approx P^{0.85}$ correlation to provide improved post-reattachment SWTBLI heating predictions as an upper limit on heat transfer rise. The ‘QP85’ correlation is not accurate within the separation bubble itself, but appears valid from reattachment onwards.

2 Discussion of Results

In the following subsection of this Results Discussion section, we first update a potentially useful incipient separation correlation for 2D compression corners so as to include the latest datasets included in the hypersonic database of Marvin, et al., [4]. An advantage of correlation ap-

proach in validating CFD, rather than just examining individual cases is that correlations can best represent collective behavior over a range of parameters. We then examine several of the 2D SWTBL interactions for their behavior with respect to Free Interaction Theory, and examine CFD/SST solutions for their compliance with both experiment and Free Interaction Theory correlations. Primary observations are made with use of the Mach 8.2 Compression Corner experimental series of Holden as it is one of the few hypersonic datasets that includes variations in both shock strength and Reynolds number. Supplemental observations (both in support of and in contradiction of these observations) of CFD results for the Mach 2.84 compression corner experimental set of Settles, Bogdanoff and Vas [10], and of the impinging shock cases of Schülein [44], [45], and of Kussoy [48] are then presented.

2.1 Incipient Separation

Important to methods used in the design and analysis of compressible flow devices is the determination of the onset of turbulent boundary layer separation. The onset of turbulent separation can have significant impact on the aerodynamic and heating performance of such flow devices, particularly those involving SWTBL interactions.

The shock strength for the onset of separation of 2D and axisymmetric SWTBLI is generally accepted to be primarily a function of Mach number, but with a weak dependence on Reynolds number. Settles, Bogdanoff and Vas [10] indicate that for a compression corner at fixed free stream Mach number, the wedge angle at which incipient separation is induced will decrease gradually with an increase in Reynolds number, but at sufficiently high Reynolds number the incipient separation wedge angle approaches a limit dependent on Mach number alone. Various authors, including Holden, Korkegi, Needham and Stollery, and Babinsky and Edwards, examining considerable supersonic data, have proposed correlations for incipient separation, giving either the shock strength, p_{inc}/p_1 , or compression corner angle, α_{inc} as a function of Mach number alone, or a combination of Mach number and Reynolds number. These correlations should be considered approximate, partly as the experimental determination of incipient separation is itself imprecise. It is useful, however, to examine the addition of the more recent hypersonic data appearing in the hypersonic SWTBLI database of Marvin, et al., [4] as compared against several of these correlations in Figs. 3 through 5. In these plots, due to the scope of this current paper, only turbulent cases are considered.

Figure 3 provides a plot of overall pressure rise through the interaction normalized by the initial wall pressure as a function of Mach number alone for the experiments in the hypersonic database of [4]. The fully separated cases are solid symbols, and the attached cases are open symbols. Also shown is a possible correlation line $((p_{inc} - p_1)/p_1 \approx$

$0.44M \exp(-M/2) + 0.13M^{2.6}$) which appears to reasonably divide the compression corner cases into either separated (above the line) or attached (below the line). This correlation line also lies close to the multi-equation correlation of Korkegi [37], not shown. Without more data such a correlation line should be used with considerable caution. The Mach 5 impinging shock cases of Schülein, however, is not so easily divided by this tentative correlation line, with one of the separated cases (10° case) being below the tentative correlation line. For the impinging shock cases, the overall pressure rise due to both the incident and reflected shock is used.

Holden [31] provides, in graphical form, a similar correlation for incipient separation for turbulent boundary layers subjected to 2D and axisymmetric Shock Wave Boundary Layer interactions. Considerable data, as of the 1977 date of that publication are also plotted in [31] that appear to confirm the validity of that correlation. This correlation has, at most, a weak Reynolds number dependence. Though not given in Ref. [31], a fit of this correlation line yields approximately the constant of 0.0165 in the equation:

$$(p_{inc} - p_1)/p_1 = M^3 C_f / 0.0165 = (2M\tau_w / (\gamma p_1)) / 0.0165 \quad (10)$$

Figure 4 plots this correlation as a dashed line, along with the fully separated data from Ref. [4] as filled symbols, and the attached data from this same database as open symbols. Unfortunately, unlike the data shown by Holden from prior to 1977, the more recent hypersonic data does not seem to be divided so distinctly by the proposed correlation line. In Figure 4, however, the value for C_f is obtained from the EddyBL/Cebeci-Smith calculations, whereas Holden either used the VanDriest II correlation or experimental values.

Figure 5 provides a plot of wedge angle as a function of Mach number and Reynolds number in the form of α/\sqrt{M} vs Re_L , similar to the plot of Needham and Stollery [38]. Incipient data from Needham and Stollery were extracted from their paper and are shown as light grey-filled symbols on this plot, as well as the additional hypersonic data from the database of [4] with attached (open symbols) and separated cases (filled symbols) identified separately. A two-part correlation line is also shown that cleanly separates the attached and separated cases. It is formed by using essentially the correlation line of Needham and Stollery, which has α/\sqrt{M} decreasing in value in the Reynolds number range of 10^6 - 10^7 , but with an extension where there is then a slight increase in α/\sqrt{M} in the Reynolds number range above 10^7 . Again, the impinging shock case of Schülein does not conform to this correlation line; the correlation should only be used with compression corner cases. The correlation line in Figure 5 (limited to 2D or axisymmetric turbulent compression corner SWTBLI in the range of Re_L between 10^6 to $150 \cdot 10^6$ and $M < 11$) is given analytically as:

$$\begin{aligned}\alpha/\sqrt{M} &= 10.25/(Re_L/10^7)^{0.11313}; & 10^6 < Re_L < 10 \cdot 10^6, & \quad (11) \\ &= 10.25 \cdot (Re_L/10^7)^{0.0089}; & 10 \cdot 10^6 < Re_L < 150 \cdot 10^6 & \quad (12)\end{aligned}$$

Data appearing in these figures indicate that these correlations are imprecise with as much as 2° scatter about the correlation lines indicating incipient separation and which divide the attached and separation cases.

2.2 Holden Mach 8.2 Compression Corner Shock/ Boundary Layer Interaction

In this subsection, reported are comparisons of our CFD solutions using both DPLR/SST and CFL3D/SST with the hypersonic compression corner shock/boundary layer data obtained by Holden at a nominal Mach 8.2 in the CUBRC shock tunnel facility. This data is reported by Holden in Ref [32] and [31], and also in the database of Marvin, Brown and Gnoffo, Ref [4]. Test data are reported for wedge angles of 27° , 30° , 33° and 36° , providing 2D flat-plate/wedge interactions ranging from attached to incipient separation to fully separated. While the reported data in Ref [32] and Ref [4] are at a single unit Reynolds number of $ReU \approx 137 \cdot 10^6/m$, Ref [31] provides additional data at two additional unit Reynolds numbers of $ReU \approx 105 \cdot 10^6/m$ and $ReU \approx 193 \cdot 10^6/m$, thereby allowing an examination of Reynolds number effects. An additional compression corner experiment of Holden at Mach 11.3 is also reported in Ref [32] and [4], giving some insight into the effects of an increase in nominal Mach number. The compression corner for the Mach 8.2 cases was located at 0.99568 meters from the leading edge of the flat plate, while for the Mach 11.3 case, the 36° compression corner was located at 1.02362 meters from the flat plate leading edge.

The nominal test conditions for the Holden Mach 8.2 compression corner cases are given in Tables 2-4, and are used for all calculations in this report. As the facility used was a shock tunnel, variations occur during and between each run. The reported run-to-run variations amounted to about 1.5% in unit Reynolds number and free stream Mach number, and $\approx 4\%$ in free stream temperature. These variations are not considered significant to the conclusions of this report. Shock relations, based on NACA 1135 relation, Ref [21], supplemented by the algorithm of Wolf [22], provide the interaction shock strength, p_2/p_1 , based on the wedge deflection angle, and are given in Table 5 for each wedge angle.

The boundaries of the grids used for the CFD solutions for the 27° through 36° Holden Mach 8.2 cases are shown in Figure 6. To reduce the impact of grid variations on the solutions, the grids for each of these cases are not independently obtained, but have common origination, in that they are generated by means of a simple rotational and stretching transformation of the Mach 11.3, 36° grid. All solutions presented

made use of grids with 513 grid points in the stream wise direction, with 189 points in the wall-normal, however checks using a higher resolution grid (1025x377) proved to demonstrate satisfactory grid convergence of solutions. The number of grid points in the span wise direction varies with the particular code used: CFL3D using 2; DPLR2D using 1; and DPLR3D using 4. As the case is 2D, the extra span wise points are obtained by addition of simple $X - Y$ planes shifted in Z . The 1st point off the wall is located typically at $y_1^+ \approx 0.1$. Transition is numerically specified to occur over the range 0.05-0.2 meters from the leading edge so as to match experimental heat transfer results.

Incipient separation for this Holden Mach 8.2 case, as evaluated, by the correlation shown in Fig. 5 should occur for a wedge angle in the range of $30^\circ \pm 1^\circ$, but see below for the discussion on sensitivity to Reynolds number.

2.2.1 Separation Sensitivity to Interaction Strength

Figure 7 depicts the experimental wall pressure distribution through the separation region in terms of the Free Interaction Variables, \mathcal{P}_ξ vs ξ for the four Holden M8.2 wedge angle cases. To accomplish this plot, the Free Interaction Theory is applied as two independent transformations:

1. The experimental wall pressure data, p_w is transformed into the normalized \mathcal{P}_ξ variable by means of Eq. 4; and,
2. The corresponding x-locations of these pressure measurements are transformed into the normalized ξ variable by means of Eq. 5.

To accomplish the transformation of Eq. 4, the upstream boundary layer wall shear stress, $\tau_{w,0}$ as obtained from the Wilcox EddyBL boundary layer code using the Cebeci-Smith turbulence model is used, rather than experimental data. Similarly, the transformation of Eq. 5, makes use of the displacement thickness, δ_0^* , from the Wilcox EddyBL/Cebeci-Smith calculations since measured skin friction and displacement thickness are typically not available for many of the experiments considered in this report. By using the Wilcox EddyBL/Cebeci-Smith results to describe the upstream boundary layer, the Free Interaction Theory approach as used within this report is truly predictive (relying on analysis without direct reference to experiment), rather than postdictive (relying on post-experiment analysis). The same nominal 2D boundary layer appears for each of these 4 wedge angles, and the EddyBL/Cebeci-Smith model is quite accurate for flat plate results with complete description of the boundary layer for these conditions. Also, by consistently using the EddyBL/Cebeci-Smith code results for the $p_w \rightarrow \mathcal{P}_\xi$ Free Interaction Theory transformations for all the cases reported in this study, the impact of experimental uncertainty of boundary layer measurements, or a lack of sufficient upstream boundary layer experimental measurements (e.g., τ_w and δ^*), on evaluation of the Free Interaction correlations is eliminated. A variation from the $x \rightarrow \xi$ transformation of Eq. 5,

is that the location of upstream influence, x_0 , from the largest wedge angle, 36° , is used when evaluating the transformation for each wedge angle, thus giving an indication of the growth of the separation extent. A curve fit of $\kappa_\xi = 0.30$ is found to be required for use in Eq. 5 for this Holden Mach 8.2 case to best fit the experimental separation pressure distributions of the 33° and 36° wedge angle cases, to the standard Free Interaction \mathcal{P}_ξ vs ξ curve, obtained from Ref [25] also shown in Figure 7. Values of $A_\xi = 5726.62$, $B_\xi = 14.55$, $p_{w,0} = 10.188\text{kPa}$, $\delta_0^* = 0.6299\text{mm}$ and $X_0 = -0.05842\text{m}$ from the 36° case are used for the transformations leading to Figure 7. These values required for the Free Interaction transformations are accumulated in Table 6 and 7, along with those quantities for the rest of the experimental cases. Also given in Table 7 is the separation wall pressure, $p_{w,s} = p_{w,0} + 4.22A_\xi$, and the separation bubble pressure plateau, $p_{w,b} = p_{w,0} + 6.0A_\xi$, obtainable by means of the Free Interaction Relations, Eqs. 4, 7 and 8.

It is seen in Figure 7, that the normalized pressure level of $\mathcal{P}_\xi = 6$ is achieved experimentally for both of the fully separated 33° and 36° wedge angle cases, with the leading edge of these normalized pressure distributions having shapes quite similar to the ‘standard’ Free Interaction Theory normalized pressure distribution shape of Erdos and Pallone (shown as a solid line). A similar but slight upward trend in normalized pressure is also observed for both these experimental cases with increasing ξ though the remainder of the separated region. The experimental scatter in pressure in the separation bubble region is fairly high at about 20%. Apparent is that the experimental 27° wedge angle case is fully attached, while the 30° wedge case is at or near incipient separation.

Figures 8-11 provide comparisons, in dimensional form, of wall pressure from RANS CFD with experimental data for the four $M = 8.2$ wedge cases of Holden. Figures 8 and 9 present results from DPLR/SST, while Figures 10 and 11 present results from CFL3D/SST. Figure 9 is an expanded scale version of Figure 8 emphasizing the separation region, while Figure 11 is an expanded scale version of Figure 10, also emphasizing the separation region. Apparent in these figures are that the solutions, in comparison to the experiment:

a. The pressure solutions through the separation bubble region, for both DPLR/SST and CFL3D/SST, agree well with both the normalized Free Interaction theory distribution and level, as well as with the experimentally observed pressure separation levels.

b. The DPLR/SST solutions consistently indicate early separation (by $\approx 3^\circ$ or 10% in wedge angle), then follows with overprediction in separation extent for each separated wedge angle, but with approximate agreement with experiment as to observed growth of separation extent with further increase in wedge angle.

c. The CFL3D/SST solutions, in contrast, agree quite well with the experimental data as to separation extent for the same wedge angle case and subsequent separation extent growth with increase in wedge angle.

d. Both DPLR/SST and CFL3D/SST indicate separation for the 30° case, whereas the experiment indicates this case is at or close to incipient separation.

e. Both DPLR/SST and CFL3D/SST post-reattachment constant pressure region levels agree quite well with the experimental data for the particular case, and also with the p_2/p_1 ratio obtained by means of the NACA 1135 relations for the primary shock system for that particular case.

2.2.2 Separation Sensitivity to Reynolds number

To examine the Reynolds variation effect additional M8.2 cases at differing Reynolds numbers for the 33° wedge angle case as presented in [31] were also calculated with DPLR/SST and CFL3D/SST. These experimental results are shown, along with experimental measurements where available, in Figures 12 through 16. In these figures, the experimental separation extent is estimated for each case by use of the pressure distribution, with separation location estimated by $\mathcal{P}_\xi \approx 4.22$. Figure 12 and 13 depict, at two Reynolds numbers, the variation of the extent of experimental separation observed with change in wedge angle or equivalently primary shock strength. Projection of the separation extent to zero so as to obtain incipient separation indicates that it occurred at approximately 29° regardless of Reynolds number in the experiment. This is in excellent agreement with the incipient separation correlation estimate given earlier.

Figure 14 also shows, for the 33° wedge angle, the significant decrease in experimental separation extent with an increase in Reynolds number. Specifically the experimental separation location, as given by $\mathcal{P}_\xi \approx 4.22$, was approximately 39.37 mm ahead of the compression corner at a unit Reynolds number of $105.6 \cdot 10^6/\text{m}$, and then decreased to 30.48 mm and 20.3 mm ahead of the compression corner at unit Reynolds numbers of $137.1 \cdot 10^6/\text{m}$ and $193.2 \cdot 10^6/\text{m}$, respectively. This represents about a 36% decrease in separation extent for a 37% increase in Reynolds number. Although the separation extent might be expected to scale with upstream boundary layer thickness (or displacement thickness, or momentum thickness), using results from Wilcox/Cebeci-Smith calculations, the upstream boundary layer thickness only decreases by $\approx 12\%$ over this Reynolds number range. Thus, the experimental Reynolds number effect on separation extent exceeds that which could be accounted for by the change in upstream boundary layer condition.

In contrast, Figure 15 shows that for the 33° case, although the DPLR/SST solutions gave larger extent of separation for these cases, the sensitivity to variation of unit Reynolds number of separation extent predicted by the DPLR/SST solutions was about an order of magnitude less, being 53.7, 51.2 and 50.7 mm ahead of the compression corner for these same unit Reynolds numbers of $105.6 \cdot 10^6/\text{m}$, $137.1 \cdot 10^6/\text{m}$ and

$193.2 \cdot 10^6/\text{m}$, shown in the figure as solid blue, black and red lines respectively. In Figure 16, the CFL3D/SST solutions, although in better agreement with the magnitude of extent of separation, also showed virtually no sensitivity to a change in unit Reynolds number, for the specified experimental unit Reynolds numbers. Unlike the Wilcox/Cebeci-Smith calculations for the upstream boundary layer at these Reynolds number levels, however, both the DPLR/SST and CFL3D/SST solutions show almost no effect on the upstream displacement thickness and boundary layer thicknesses, and only a small effect on the momentum thickness. Figure 17 provides velocity and temperature profiles for the upstream boundary layer at two of the Reynolds number levels, as obtained from the DPLR/SST solutions, and indicate that the boundary layer thickness undergoes little change with the increase in Reynolds number; rather, the effect of change in Reynolds number mostly affects the inner portion of the upstream boundary layer for the RANS solutions. It is anticipated that deficiencies in turbulence modeling that primarily affect the inner boundary layer will be most felt in surface heating and shear stress, whereas changes in modeling so as to improve predictions of the extent of separation would require addressing the entire boundary layer.

To explore further the reduced sensitivity by RANS/SST of separation extent to changes in Reynolds number for this Mach number and wedge angle, two additional cases were constructed, similar to the experimental Reynolds number variation but with a wider change in Reynolds number. These additional ‘constructed case’ results are also shown in Figures 15 and 16 for DPLR/SST and CFL3D/SST calculations at these two additional Reynolds numbers. In Figure 15 and 16, these additional cases are shown as the dashed blue line which represents a unit Reynolds number of $137.1 \cdot 10^6/\sqrt{10}/\text{m}$ (or $13.2 \cdot 10^6/\text{ft}$), and the dashed red line representing a unit Reynolds number of $137.1 \cdot 10^6 \cdot \sqrt{10}/\text{m}$ (or $136 \cdot 10^6/\text{ft}$), thereby giving an order of magnitude overall change in Reynolds number, centered about the middle experimental Reynolds number. This larger Reynolds number variation represents about a 5x larger variation than was explored in the experiment, but seen is that the increase in separation extent over this larger range approximated that seen in the experiment. Thus with the wide spacing in Reynolds number, the RANS/SST solutions provide only 20% the sensitivity of separation extent to Reynolds number than that seen in the experiment. This low sensitivity of RANS/SST calculated separation extent to Reynolds number could prove problematic in optimization design procedures of such devices as either hypersonic control surfaces or scramjet inlets, both devices making use of compression corners. Of some further concern to hypersonic design methods use of embedded RANS/SST analysis is that with the more narrow spacing in Reynolds number spacing (at the widest experimental values of Reynolds number), the sensitivity of separation extent to Reynolds number for the RANS/SST solutions is even smaller, $\approx 10\%$ of the experimental sensitivity. Thus, the RANS/SST sensitiv-

ity of separation extent to Reynolds number is not even consistent over the Reynolds number range observed. Effectively this is a form of ‘digital noise’ as can sometimes be generated by numerical differentiation of closely spaced inputs, and which to some MDO optimization methods could prove unstable. Whether experiment or CFD, certain quantities of interest such as separation extent or wall heating can be subject to run-to-run variation, and place a lower practical limit on how closely spaced input test conditions should be set before running the risk of the desired observation of parametric trends sinking into the background level of run noise.

The DPLR/SST solutions indicate early separation (by $\approx 3^\circ$ or 10% in wedge angle) with reduced Reynolds number sensitivity, but with approximately the correct separation extent growth per degree of wedge angle. The CFL3D/SST solutions also exhibit low response of separation extent to change in Reynolds number. In contrast to the DPLR/SST solutions, the CFL3D/SST solutions do indicate good agreement with experiment as to the separation extent along with the correct growth of separation extent per degree of wedge angle. This differing behavior between the two codes might suggest that the implementation of the SST model in these two codes differ in some significant way. However, options available to each code were exercised to ensure quite similar set of assumptions (e.g., Vorticity-based production vs. ‘Exact’ production, 1st vs 2nd order accuracy, etc.), with each of these options having insufficient effect to explain the offset in separation onset or insufficient Reynolds number parametric trend. We observe that for strong viscous/inviscid interaction flows such as these compression corner shock cases, however, the physics effects of both viscous and inviscid effects are present and competing for dominance. Thus, it is best to consider not just the viscous implementation but that differences between these two codes in numerical modeling exist for both the viscous and inviscid physics and may prove of equal importance.

2.2.3 Mach Number Sensitivity

Holden also provided a 36° Mach 11.3 fully separated compression corner related to the Mach 8.2 cases. Only the single fully separated case is available experimentally. As a consequence, Incipient separation is not determined experimentally for this case, but a comparison of DPLR/SST and CFL3D/SST with experimental results can prove of value in considering sensitivity of the turbulence model accuracy to Mach number variations. A comparison of Figures 18 and 19 for wall pressure, indicates that, as with the Mach 8.2 Holden cases, the DPLR/SST solution overpredicts the separation extent by $\approx 100\%$, while the CFL3D/SST solution is in excellent agreement with experiment. Also due to there being only a single experimental case, no evaluation of sensitivity of the extent of separation to change in shock strength, compression corner an-

gle, nor to Reynolds number effects can be made. The utility of adding additional runs for such effects, accomplished at little extra effort or cost, should be obvious to future experimenters.

2.2.4 Wall Heating

Figures 20 through 22 depict comparisons, for the Holden Mach 8.2 27° - 36° wedge angle cases at the unit Reynolds number of $137.1 \cdot 10^6/\text{m}$ condition, of wall heating distributions from DPLR/SST computations with experimental measurements and the $(Q/Q_0) \approx (p/p_0)^{0.85}$ correlation of Back and Cuffel [30]. The ‘QP85 heat transfer’ distributions shown in these figures, are based on the Back and Cuffel correlation and rely on the wall pressure distributions of Figure 8. The overprediction of separation by the DPLR/SST computations is evident in these figures, but evident also is the nearly 50% overprediction or spike in the wall heating past reattachment for those cases where separation occurs. For the attached case of 27° wedge angle, the RANS solution prediction of wall heating agrees with the heat transfer derived from the QP85 correlation from the experimental pressure measurements, while being consistently high relative to the experimental wall heat transfer measurements. Either the QP85 correlation- in which there has proven to be some confidence outside the separation region- is proving to be too high for these cases by $\approx 25\%$, or it is the experimental heat transfer measurements that are too low. But for the fully separated cases of 33° and 36° wedge angle, the wall heating is underpredicted through the separation region along with the $\approx 50\%$ overprediction spike in wall heating peak. Once the post-reattachment constant pressure region is reached, a discrepancy in wall heating, between experimental measurements and RANS solution, is limited to $\approx 20\%$.

2.2.5 Comments on Observed Turbulence Model Deficiencies

From the above observations of SST calculations for the Holden SWTBL interaction cases, and from observations previously reported by Brown [2], several deficiencies in SST model applied to hypersonic SWTBLI seem clear:

1. Overprediction by the standard SST model for the Wall Heating spike past reattachment;
2. Overprediction by the standard SST model for the Separation extent for SWTBLI cases;
3. Lack of proper sensitivity to Reynolds number as to separation extent;
4. Wall Heating for ‘acreege’/upstream flat plate boundary layer regions is $\approx 10\%$ high for SST model relative to experiment; and
5. Grid Sensitivity of the standard SST model (at larger y^+ values).

To explore a possible basis for some of these turbulence model deficiencies, Figures 23 through 25 are provided for the Holden Mach 8.2 36° case of the DPLR/SST solutions. Figure 23 depicts a streamline array (in red lines) originating in the upstream boundary layer in the vicinity of separation. Note this upstream boundary layer streamline array lifts over the recirculation region and reattaches past the compression corner. Plots of the turbulent kinetic energy development and of the eddy viscosity along the individual streamlines (as a function of X) of this streamline array are provided in Figures 24 and 25. The individual streamlines are labeled with their initial upstream boundary layer distance from the wall in millimeters. In both Figures 24 and 25, the response of the turbulent field in progressing from the upstream boundary layer (marked as BL in Figure 23) to the initial λ -shock (marked as λ) seems slow, particularly compared to the later growth while the viscous layer develops as an adverse pressure wake region located above the recirculation region, and then followed by a rapid further growth of the turbulent field to the compression or reattachment shock (marked as C in Figure 23). The eddy viscosity does rise gradually from $X=-0.1$ m to -0.05 m, but the reattachment shock in the vicinity of $X=0.05$ gives rise to a substantial rise in eddy viscosity as reattachment is approached.

It is clear that although the SST turbulence model may well mitigate the buildup of the turbulent field in the vicinity of reattachment (relative to other two-equation models), as is suggested by Menter and Esch [35], the problem of high eddy viscosity levels at reattachment remains for these hypersonic turbulent separating/reattaching SWTBLI cases.

To address the model deficiencies enumerated above might require a more substantial development of eddy viscosity in the early phases of separation to promote resistance to separation, while near reattachment the effect of the high levels of eddy viscosity on heat transfer would need to be moderated. The overprediction of heat transfer in the vicinity of reattachment, where eddy viscosity is high suggest the strong linking of turbulent momentum and energy transport implied by the use of constant turbulent Prandtl number in the current form of the SST model be replaced by an alternate approach where either separate modeling for the turbulent heat transfer, or of a variable turbulent Prandtl number be introduced. Essentially, the turbulent eddy diffusivities for momentum and heat transfer appear to no longer be closely linked through the SWTBLI separation and reattachment processes and are inadequately represented in the non-equilibrium regions by a simple constant turbulent Prandtl number. Efforts along these lines have been conducted by Sommer, So and Zhang [41], by Xiao, Edwards and Hassan [42] and by others. Additionally, implementation of realizability constraints and Explicit Algebraic Reynolds Stress modeling may well promote a more accurate development of the turbulent field at both separation and reattachment.

2.3 Settles Mach 2.84 Compression Corner Shock/ Boundary Layer Interaction

The Settles experiment provides cases with a variation in shock strength for an adiabatic wall 2D compression corner at low supersonic Mach number of 2.84, which we examine to contrast with observations we have made from the hypersonic Mach 8.2 results for Holden. As with Holden’s experiment, the parametric variation provided for by Settles [8, 11] included a variation in shock strength from attached through incipient separation to fully separated; but, was conducted at only a single reported Reynolds number, and a single reported Mach number. An earlier publication of Settles [10], however, describes a more extensive dataset—mostly provided in non-dimensional analyzed form—that does include a considerable variation in Reynolds number. The lower supersonic Mach number of this case, relative to Holden, allows for the potential of a more accurate inviscid contribution to a CFD solution since numerical inaccuracies associated with inviscid total Pressure loss through the shock structure will likely have reduced impact on the numerical accuracy of the overall CFD solutions. Furthermore, as it is an adiabatic wall supersonic case, the accuracy of heat transfer modeling should play a reduced role in overall accuracy of CFD solutions.

Navier-Stokes solutions were accomplished for the Settles configuration and test conditions using both DPLR and Cf3d with the SST two-equation turbulence model. The grids were a single block of 1025x289 grid points and are based on a simple geometric transformation of the same basic compression corner grid shown in Figure 6 and mentioned previously in the Holden section above, but adjusted for test plate length, grid spacing at the wall and wedge angle to conform to requirements for the Settles cases. The grid spacing at the wall was $y_1^+ \approx 0.05$.

As the Settles test was run with a wedge mounted on a wind tunnel wall rather than on a flat plate suspended in the wind tunnel, it was necessary to adjust the flat plate run length for the CFD grid so as to result in a best match the measured upstream boundary layer properties. As a consequence, the CFD grid was set at $L = 1.8\text{m}$ (similar to the 1.98m nozzle to wedge run length in the experiment) with EddyBL/Cebeci-Smith computations giving $\tau_w = 145\text{ Pa}$, $\delta_o = 23.7\text{ mm}$, $\delta_o^* = 6\text{ mm}$ and $\theta_o = 1.15\text{ mm}$ compared to the experimental measured $\tau_w = 141.7\text{ Pa}$, $\delta_o = 23.0\text{ mm}$, $\delta_o^* = 6.1\text{ mm}$ and $\theta_o = 1.2\text{ mm}$ for the 20° case (measurements for the other wedge angles differed slightly).

First, discussing aspects of the Settles experiment, we consider the interaction strength for onset of separation. In Settles experiment, the 16° case is reported to be ‘nearly incipient separation’, while the 20° and 24° cases are reported as fully separated. By the correlation shown Figure 5, the incipient separation demarcation would occur at $\alpha_i \approx 10.25\sqrt{M_e} \approx 17.3^\circ$, within range of accuracy of that correlation. DPLR/SST solutions were obtained at various wedge angle cases for the Settles exper-

iment and intervening wedge angles as well, with the onset of separation occurring at 14° (not shown), approximately $2 - 3^\circ$ early, similar to the performance of DPLR/SST solution for the Holden experiment. The role of inviscid modeling inaccuracies relative to viscous modeling is likely reduced for the Settles case compared to the Holden; hence, it appears likely the nearly constant 3° of early incipient separation seen in DPLR/SST across this wide Mach number range points to the SST model or its implementation.

Next, the Free Interaction transformed pressure distribution is presented in Figure 26, for Settles experimental measurements of the fully separated 20° and 24° wedge angles. As can be observed, the experimental wall pressures in the separation bubble region conform quite well to the pressure levels and leading edge shape of transformed pressure distribution. In terms of the transformed variables, the growth of the separation extent over the range of this 4° increase in wedge angle corresponds to $\Delta\xi \approx 0.5$, giving $\partial\xi_0/\partial\alpha_i \approx 0.125$, which considering the low accuracy of the curve fit of the ξ transformation, is within range of the $\partial\xi_0/\partial\alpha_i \approx 0.3$ seen in Figure 7 for the Holden cases.

Figure 27 compares the DPLR/SST and experimental wall pressure distributions for the Settles 16° , 20° and 24° cases. Indicated is that, as with the Holden Mach 8.2 case, DPLR/SST is predicting early separation by about 3° , or $\approx 10\%$ in wedge angle. Others, e.g. Ref. [50], also show the SST model as over-predicting the separation extent for the 24° Settles case (note, in Ref [50] their separation extent for their calculations and reference to the experiment appears to be in terms of x/δ , with $\delta = 2.3\text{cm}$ from the paper by Settles [11]). However, Figure 28 demonstrates that this early separation leads to a quite similar overprediction of separation for the fully separated 20° case for both the DPLR/SST and Cfl3d/SST solvers. This is in contrast to the results for the Holden Mach 8.2 case for DPLR/SST vs Cfl3d/SST results shown in Figure 9 vs Figure 11, in which is indicated that although the DPLR/SST overpredicts separation comparable to an increase in wedge angle by 3° , the Cfl3d/SST solver was quite accurate as to separation extent. Thus, the over-prediction in separation extent shown by DPLR/SST is consistent across these two cases, while the Cfl3d/SST prediction varies in its accuracy. Among the possible reasons for this is the acknowledged experience that the SST model tends to overpredict separation, but this may in part be offset by different inviscid modeling of these two codes in their ability to deal with the weaker vs stronger shocks of Settles vs Holden cases. The DPLR/SST results are more consistent in overprediction regardless of the shock strength, while the Cfl3d/SST results seem to actually improve with increase in shock strength. For these strong interaction flows, it is both the inviscid numerical implementation and the viscous numerical implementation which must interact together with accurate modeling of all physical features of the SWTBL interaction.

In Figures 29, 30 and 31 is explored the sensitivity of the separa-

tion extent to Reynolds number variation. Figure 29 presents, in non-dimensionalized form, separation extent data and correlation extracted from Figure 17 of Ref. [10] and which incorporates both Reynolds number and wedge angle effects for the Settles Mach 3 compression corner experiments. This correlation should still apply to the later data of Ref [11]. Figures 30 and 31 provides a comparison of the measured wall pressure distribution in the vicinity of separation of the 20° case from Ref. [11] with computed wall pressure distributions obtained with DPLR/SST and Cf3d/SST, for the single Reynolds number of that dataset, but supplemented by additional Reynolds number cases which should be addressable by means of the Settles correlation.

Figure 29 describes Settles 1975 data’s non-dimensionalized upstream influence extent dependence on both Reynolds number and wedge angle in one plot, along with a correlation for these variables specific to Mach ≈ 2.84 Settles experiments. The range of Reynolds numbers runs from $Re_{\delta_0} = 0.52 \cdot 10^6$ to $7.64 \cdot 10^6$ (with Re_x up to $\approx 10^9$), and wedge angles from 10° to 20° . ‘Upstream influence’ extent is as obtained from measured wall pressure distributions as the location in front of the compression corner at which the interaction pressure rise begins (see Ref. [10] for details), and is presented in non-dimensional form as $\Delta X/\delta_0$. The B variable in this figure characterizes the wedge angle and Reynolds number of the particular case through the definition:

$$B \equiv \alpha + 20. - 1.26 \cdot \log Re_{\delta_0} \quad (13)$$

The correlation that Settles obtained, was:

$$\Delta X_u/\delta_o \equiv 0.03 + 0.0016 \cdot e^{0.288 \cdot B} \quad (14)$$

Emphasis must be made that this correlation should only be considered as verified for use with Settles $M \approx 3$ data. We should be able to make use of this correlation, however, to ‘extend’ the single Reynolds number for the 20° separated Settles case as considered in Figures 30 and 31 to cover a range of Reynolds numbers (where the single experimental Reynolds number is scaled by $0.316x$, $0.562x$, $1.778x$ and $3.16x$ for ‘constructed cases’ as well as the actual single measured Reynolds number as used from Ref. [11] and labeled as Re1.000x in these figures).

Considering, then Figures 30 and 31, computed wall pressure distributions from both DPLR/SST and Cf3d/SST for the 20° case agree with each other for the measured Re1.000x case and as to the additional ‘constructed’ Reynolds, in that they both overpredict the extent of separation in the measured Re1.000x case by effectively $\approx 3^\circ$ in wedge angle, and also as to the effect that the constructed Reynolds number cases influence their extent of separation observed in the wall pressure distributions. This is in contrast to the Holden Mach 8.2 case considered previously(contrast Figs 30 and 31 with Figs 15 and 16), where the

experimental Reynolds number sensitivity of separation extent was not observed by RANS/SST.

To determine whether the magnitude of Reynolds number sensitivity is consistent with the Settles correlation, we apply the Settles correlation so as to determine the anticipated upstream influence extent for these cases. Relative to the Reynolds number of the measured 20° case of Settles [11], the ‘constructed cases’ computed in Figs 30 and 31 have Reynolds numbers of $Re = 0.3162x, 0.562x, 1.000x, 1.778x$ and $3.162x$ or a variation in Reynolds number of $\pm 1/2$ order of magnitude. By the correlation of Settles, the relative extent of the separated region for these cases should be $\Delta X/\Delta X_{Re1.000x} \approx 1.634, 1.277, 1.000, 0.7721$ and 0.6071 , respectively. In Figure 30 for DPLR/SST and Figure 31 for Cfl3d/SST, the computed separation extent is slightly larger than these values by a mere $\approx 10\%$. Thus, at Mach 2.84, the computed separation extent is slightly more sensitive to Reynolds number variation, whereas, in contrast, for the Mach 8.2 Holden case the computed separation extent was inaccurate and quite insensitive to Reynolds number variation.

Another observation available from Figures 27-31, is that the magnitude of the DPLR/SST and Cfl3d/SST computed wall pressures in the separation region agree quite well with the corresponding experimentally measured wall Pressure magnitudes, and also the pressure levels (either $p_{w,b} \approx 46.476\text{kPa}$ or equivalently $p/p_0 \approx 1.97$) that should occur from Free Interaction Theory for the Settles experimental conditions as indicated in Table 7. Overall the Settles Mach 2.84 cases appear to be reasonably well predicted by both the DPLR/SST and Cfl3d/SST methods, except for early incipient separation, followed by a nearly constant overprediction in separation extent.

However, the troubling change in Reynolds number sensitivity behavior, from well-behaved at Mach 2.84, to inaccurate at Mach 8.2 is significant to potential use of so-called high-fidelity Physics based methods (RANS) in design and MDO methods. This Reynolds number sensitivity inconsistency with Mach number is not fully understood at this time, but none of the possible origins can be eliminated, whether traceable to viscous or inviscid modeling applied to the interaction or the upstream boundary layer computations, or even grid requirements. DPLR/SST exhibits a consistent early incipient separation by $\approx 3^\circ$ in wedge angle, whereas there is an actual improvement in Cfl3d/SST where at Mach 2.84 early separation by $\approx 3^\circ$ exists, but which does not appear at Mach 8.2.

2.4 Schülein Mach 5 Impinging Shock/Boundary Layer Interaction

The Schülein impinging shock/boundary layer interaction flow topology is shown in Figure 2. This experiment (reported in Refs. [44] and [45], also in the database [4]) was conducted at a fixed unit Reynolds number

of $38.8 \cdot 10^6/\text{m}$, and Mach number 5. A 2D boundary layer developed on the test surface consisting of a flat plate with a shock generator positioned above the flat plate and inclined so as to generate a shock that impinged on the flat plate boundary layer at approximately $x = 0.35\text{m}$. Various shock angles of 6° , 10° and 14° were generated so that impinging SWTBL interactions occurred on the flat plate ranging from attached to incipient separation to fully separated. Nominal run conditions for the Schülein experiment are presented within the Tables 1-3. The several cases primarily differed in shock strength only, with no deliberate variation in Reynolds number nor Mach number.

Extensive examination of DPLR/SST solution uncertainty for this flow was examined in the prior publication by this author [2, 3], as well as by others, e.g., Fedorova, et al., [46] and Zhang, et al., [50]. (Note that Zhang, et al., use of ‘ x ’ appears to be actually the non-dimensionalized x/δ_0). In this subsection we provide additional examination of the experiment with respect to the Free Interaction Theory formulation, and of comparisons with both DPLR/SST and CFL3D/SST solutions.

The DPLR/SST and Cf3d/SST solutions were accomplished with the grids reported and available from Ref. [4]. These 3 block grids, being 1056x256 cells for the 6° fine-grid case, 528x128 cells for the 6° medium-grid 6° and 10° case, 1056x256 cells for the 14° medium-grid case, and 2112x512 cells for the 14° fine-grid case. The number of cells span wise depended on grid requirements of each particular code for these essentially 2D cases.

Figure 32 presents a comparison of the Free Interaction transformed experimental wall pressure distribution, \mathcal{P}_ξ vs ξ , for the fully separated 14° impinging shock case with the nominal theoretical distribution. Note the experimental \mathcal{P}_ξ distribution does demonstrate a continued slight rise rather than a strictly constant level past separation ($\mathcal{P}_\xi \approx 6$, See also Fig. 26; however, within the accuracy of the fit, and of the experimental wall pressure accuracy, the experimental wall pressure nearly follows the ‘ideal’ Free Interaction wall pressure distribution shape and magnitude within the separation region. This helps to substantiate the accuracy of the experimental separation region wall pressure measurements, inasmuch as the computed DPLR/SST and Cf3d/SST separation wall pressure levels are observed from Figs 33 and 34 to both be significantly lower ($\approx 1/2 - 2/3$) relative to the experiment. This behavior of low computed separation bubble pressure is seen to be consistent with virtually every other Navier-Stokes/SST computation for this case, e.g. Steelant [51] and Kovar [52], except that of Fedorova, et al., [46, 47]. Figure 33 shows the DPLR/SST wall pressure distribution comparison from DPLR/SST solutions with experiment for all three of the impinging shock generator cases, 6° , 10° and 14° . Figure 34 provides a comparison of DPLR/SST and Cf3d/SST wall pressure distribution with experiment for the 14° case. Seen is that the only significant region of disagreement in wall pressure distribution between CFD and experiment is for the separation

region. In the separation region, DPLR/SST and Cf3d/SST both underpredict the pressure level by approximately 35% – 50%, and, unlike the compression corner cases discussed above, both slightly underpredict the separation extent.

All three experimental cases, whether attached or separation, exhibit a rise in pressure through the interaction region to an extended post-reattachment region of constant pressure level within excellent agreement of the inviscid level predicted by simple inviscid analysis of the 2-shock (impinging and reflecting shocks) problem, see Brown [3] for further description of the double-shock solution. Using the p_2/p_1 analysis entries from Table 5 for each of these cases, this post-reattachment region pressure level should be by inviscid analysis: 16.19kPa for the 6° case, 32.82kPa for the 10° case, and 58.68kPa for the 14° case. In Figure 33, experimental and CFD wall pressures within this extended post-reattachment constant pressure region are in excellent agreement amongst each other and as to the inviscid double-shock problem analysis. This extended post-reattachment constant pressure region is terminated (with decreasing wall pressure) by the expansion fan emanating off the shock generator trailing edge. Thus, the ‘footprint’ of the region between where the impinging shock impinges the boundary layer ($x \approx 0.35\text{m}$ for all three cases) and the earliest impingement of the expansion fan (for the 14° case at $x \approx 0.45\text{m}$) is about a duration of 0.1 meters minimum, or about $L_{interaction}/\delta_o \approx 21$, using $\delta_o = 4.813\text{mm}$ from Table 4. This appears to be sufficient stream wise distance required for the interaction region to express full development of the various flow structures-including separation and an extended post-reattachment constant pressure region. Hence, we refer to this case of Schülein as being a ‘long’ or ‘fully developed’ impinging SWTBLI. We will briefly show an example of a ‘short’ or ‘early termination’ impinging SWTBLI in the next subsection.

Figures 35-37 depict comparisons of wall heat transfer distributions for the three experimental cases. Figure 35 compares the DPLR/SST computed wall heat transfer distributions with the experimental measurements. Figure 36 compares the wall heat transfer as computed from DPLR/SST wall pressure results based on the QP85 correlation with experimental measurements. And, finally, in Figure 37, a comparison of QP85 correlation based wall heat transfer is presented based on both the DPLR/SST and measured experimental wall pressure distributions. What is clear from these three figures is that, the measured wall heat transfer throughout most of the interaction is better predicted-based on DPLR/SST pressures-by a post-analysis using the QP85 correlation than by direct use of wall heat transfer results from the DPLR/SST solutions, see also Brown [3]. The direct wall heat transfer predictions by DPLR/SST is seen to produce an overshoot by nearly 50% past reattachment for the separated case, before following a downward trend-yet remaining well above-the measured wall heat transfer throughout the post-reattachment constant pressure region. The wall heat transfer within the

separation region is not predicted by either the direct DPLR/SST wall heat transfer results, nor the wall heat transfer obtained by the QP85 correlation whether from the DPLR/SST solution or as an indirect inference from measured wall pressures. The QP85 correlation should not be used within the separation region, but post-reattachment seems to perform better than the current state-of-art in CFD turbulence modeling for wall heating. We do observe in Figures 35 and 36 that the measured wall heat transfer, particularly for the 14° case undergoes a gradual decline in magnitude throughout the post-reattachment constant pressure region. This is likely due to a natural stream wise development of an otherwise nearly equilibrium boundary layer-with increase of boundary layer thickness and consequent reduction of wall heating- occurring for this constant pressure region.

To explore the possible physical basis for the low separation pressure, as well as for the post-reattachment wall heating overshoot, we consider the contour plots in the region of the Schülein 14° interaction from both DPLR/SST and Cf3d/SST solutions presented in Figures 38 and 39. These two plots are Pressure contour plots (flooded contours in color, with solid black contour lines), supplemented by streamlines in red. Figure 38 shows an expanded scale of the DPLR/SST separated region, while Figure 39 shows (to the same expanded scale) of the Cf3d/SST separated region. The Cf3d/SST pressure contour plot is shifted slightly in X by 4mm to a lower X value to account for the Cf3d/SST separated region being located slightly earlier than is the DPLR/SST separated region. The size of the two separated regions are actually quite similar. The shift to lower X of the Cf3d/SST separated region is due to the inviscid solver of Cf3d generating a somewhat steeper shock than does the inviscid solver of DPLR.

The flow topology of these two solutions is generally quite similar, but differ in detail. Of particular note in both of these contour plots are the 4 streamlines in red that are placed at the same location in the upstream boundary layer: $Y_0 = 1, 2, 3$ and 4 mm away from the wall, starting at $X = 0.316\text{m}$. In both these contour plots, these streamlines demonstrate the upstream boundary layer lifting away from the wall at separation, being turned by the λ -shock so as to become a wake-like viscous layer bounding the recirculating region from above, encountering the shock triple point, then followed with an expansion wave just past the peak height of the recirculating region, where the wake-like viscous layer is turned sharply back to the surface to close the recirculating region at the reattachment point. The reattached boundary layer past reattachment is significantly reduced in thickness (along with the increase in density) compared to the upstream boundary layer, and encounters an adverse pressure gradient as it continues past reattachment.

Correct computation of this sequence of events places a considerable challenge on both the viscous and inviscid numerical modeling. It can be seen from the pressure color flooded contours past the expan-

sion wave, that the separation bubble pressure appears to be consistent with and possibly established by the pressure level (seen in ‘light blue’ in these color flooded contour plots) generated ‘above’ and to the ‘back-side’ of the recirculating region as the separated viscous wake traverses between the expansion wave and the reattachment point. As to the inviscid solvers, DPLR and Cfl3d, more detail and a higher peak pressure seems to be generated by Cfl3d just past the expansion wave and above the recirculation region, as experienced by the 4 streamlines in red being discussed. These two codes differ as to inviscid flux function, DPLR being a modified Steger-Warming, while Cfl3d solutions used a mixed Roe-Van Leer formulation.

While the inviscid formulation of these two solvers accounts for some of the differences between their solutions in the separated region, another apparent possible source of discrepancy between the CFD solutions and the experiment likely to arise is from the extensive turning occurring with the streamlines in the vicinity of the pressure peak at the triple point-expansion wave region located at the peak of the recirculation region. This extensive turning by this viscous layer suggests the need for curvature terms to be incorporated into the turbulence modeling, not present in either the DPLR or Cfl3d SST formulations. Whether incorporation of curvature terms into the turbulence model would improve the separation bubble pressure prediction is yet to be explored.

Another concern is the overshoot in wall heating past the reattachment location (at about $x = 0.36\text{m}$). Figure 40 attempts to explore that issue, supplementing information observable in Figure 38. Again we refer to the 4 streamlines located in the upstream boundary layer visible in Figure 38, and located initially at $Y_0 = 1, 2, 3$ and 4 mm away from the wall, starting at $X = 0.316\text{m}$. Note the curve associated with the streamline closest to the wall (labeled $Y_0 = 1\text{mm}$) is colored black in Figure 40, while the rest are colored red, to facilitate deciphering the plot. Figure 40 follows the development of DPLR/SST turbulent kinetic energy along each of these streamlines through the interaction region from $x = 0.3\text{m}$ (before separation at $x \approx 0.32\text{m}$) to past reattachment (at $x \approx 0.35\text{m}$ and past the wall heat transfer overshoot (at $x \approx 0.36\text{m}$). Seen is a rapid growth in turbulent kinetic energy as the viscous layer first separates then converts into a wake-like viscous layer experiencing first the λ -shock followed by a slight adverse pressure gradient. A slight decrease in TKE then occurs at about $x = 0.34$, believed to be associated with favorable pressure gradient experienced at the upper boundary of the recirculating region, followed by a rapid increase in TKE as the adverse pressure gradient is encountered by these streamlines as they approach the reattachment location.

An unfavorable feature of two-equation eddy viscosity models is their over-prediction of turbulent energy production in encounters with decelerations involving predominately normal strains such as shocks, stagnation and reattachment points. A primary contributing factor to this

overproduction is that two-equation ‘K’-based models, of necessity, assume the normal stresses are isotropic, which when simply multiplied by the divergence of the velocity field numerically produces a high turbulence production. In contrast, a realistic turbulence field -anisotropic and subject to realizabilty constraints- subject to pure normal stresses will produce a considerably lower turbulence production. Coupled with the oversimplification of the connection of eddy diffusivity for momentum transfer to heat transfer invoked by the use of a constant turbulent Prandtl number, it is not surprising that the overshoot in wall heating past reattachment occurs.

Additionally, Simpson [53] established the important role that the difference in normal stresses, $(u'^2 - v'^2)$, and not just the shear stress $u'v'$, can play in both the momentum and turbulent equations for the two-dimensional separation process. Conventional two-equation models, of course, will incorrectly yield zero for such normal stress formulations.

By these observations and physical arguments, it seems unlikely that simple modifications to two-equation eddy viscosity models, such as for even the SST model, making use of constant turbulent Prandtl number will lead to a robust physically accurate prediction of wall heating near reattachment points. At present the simplest advanced anisotropic modeling of turbulent fields appears to be EARSm models such as that of Wallin and Johansson [54], or Hellsten [55, 56]. To decouple the eddy diffusivity for momentum and heat transfer in a manner more advanced than a simple constant turbulent Prandtl number has been examined by, for example, Xiao, et al., [42, 43].

2.5 Kussoy Mach 8.2 Impinging Shock/Boundary Layer Interaction

In this subsection, we briefly examine the Kussoy Mach 8.2 Impinging Shock/Boundary Layer Interaction as an example of a ‘short’ or ‘premature termination’ Impinging SWTBLI, so as to contrast with the Schülein ‘long’ or ‘fully developed’ Impinging SWTBLI.

The experiment of Kussoy and Horstman, Ref [48], is that of a 2D hypersonic impinging shock generated by a tilted flat plate placed above a flat plate test surface. The test was conducted at a nominal Mach number of 8.2, with interactions ranging from attached to incipient separation to fully separated provided by variety of shock generator angles: 5° , 8° , 9° , 10° and 11° . For the purposes of this report, we restrict ourselves to the 10° fully separated case, conducted at test conditions (given in Tables 1-3 for the B3.Kussoy entry). The test unit Reynolds number was $4.91 \cdot 10^6/\text{m}$, with the shock impingement occurring at about $x = 0.31\text{m}$. The upstream wall pressure was $p_1 = 430\text{Pa}$, total Pressure was $P_T = 24.95\text{MPa}$. Kussoy reports the experimental upstream wall heat transfer as $Q_0 = 1.04\text{W}/\text{cm}^2$, while the EddyBL/Cebeci-Smith boundary layer code gives $Q_0 = 1.128\text{W}/\text{cm}^2$. Kussoy also reports the

experimental boundary layer thickness, $\delta_0 = 37\text{mm}$ and $\delta_0^* = 15.9\text{mm}$, while the corresponding EddyBL/Cebeci-Smith values (from Table 4) are $\delta_0 = 39.6\text{mm}$ and $\delta_0^* = 17.7\text{mm}$, and from Figure 41, the DPLR/SST boundary layer thickness is $\delta \approx 21\text{mm}$. Because the actual test geometry was being calculated (unlike the Settle test conducted on a tunnel wall), no closer match in upstream boundary layer properties was attempted.

Figures 42 and 43 (from Ref [2,3], compare wall pressure distributions and wall heat transfer distribution respectively, for DPLR computations with several turbulence models, including SST, against the experimental data obtained by Kussoy. Excellent agreement as to the pressure distribution between computations and experiment is observed, except for details in the separation region. The separation extent for SST is about 2/3 of that obtained in the experiment. Also the SST separation bubble appears to be low relative to the experimental level. Good agreement as to the wall heat transfer distribution is seen in Figure 43 between the computations and measurements, except the the peak value for SST model results exceed the peak value from measurements by approximately 30%. However, in contrast to the the ‘fully developed’ Schülein wall pressure distributions which exhibit an extended post-reattachment region of constant wall pressure corresponding quite accurately to the pressure rise through both the impinging and reflected shocks, the Kussoy wall pressure distribution, of Figure 42, does not exhibit such behavior, being more of a bell-shaped curve for both wall pressure and wall heating. For the Kussoy 10° case, we anticipate the double or impinging/reflection shock pressure rise to result in a value (from Table 5) of approximately $p_2/p_1 = 19.155$. This rise in pressure ratio level is just reached in Figure 42, but immediately followed by a rapid decline.

The Pressure and Mach contours of Figure 44 and 45 explore why the anticipated region of constant high pressure does not occur for the Kussoy experiment. Both of these figures concentrate on the flow interaction about the separation/reattachment region, extending from before where separation occurs (at $x \approx 0.28\text{m}$) and the impinging shock encounters the outside edge of the boundary layer (at $x \approx 0.308\text{m}$) until just past where the wall pressure peak is observed (at $x \approx 0.41\text{m}$).

Note, observable in both Figures 44 and 45, is that the expansion fan from the trailing edge ($[x, y]_{TE} \approx [0.3, 0.048]\text{m}$), first encounters the reattaching boundary layer edge in the immediate vicinity of the wall pressure peak (at $x \approx 0.41\text{m}$). The interaction, which extends from $x = 0.28\text{m}$ to $x \approx 0.41\text{m}$ has just sufficient downstream development distance available to reach the full pressure rise before the expansion fan ‘terminates’ the interaction. Thus, this Kussoy case is not truly ‘prematurely terminated’ by the expansion fan, but rather is at the defining edge between ‘fully developed’ and ‘prematurely terminated’. Were the Kussoy 10° shock generator any shorter, there would not likely have been full development and the full pressure rise would not have occurred. Regardless, there is not sufficient development length available for a post-

reattachment constant pressure region similar to that of Schülein case to occur.

As a further observation, an attempt to fit the experimental wall pressure distribution in the separation bubble by means of the Free Interaction Theory transform equations similar to the prior discussions with Holden, Settles and Schülein, failed for this ‘short’ impinging shock interaction. Possibly this is because the reflected (or reattachment) shock observed in Figures 44 and 45 is distorted by the close proximity to the expansion wave leading to the back-side of the separation bubble to be bounded by relatively lower pressure ($p_b \approx 1\text{kPa}$) than would otherwise occur ($p_{w,b} \approx 2.2\text{kPa}$ by Table 7 for Free Interaction Theory). This case does not seem to fit well with the standard Free Interaction theory due to the early termination of the interaction by the Trailing edge expansion fan leading to a distortion of the reflected shock and related flow on the backside of the separation bubble and the consequent absence of a developed post-reattachment constant pressure region. Note that the distance along the test surface between the footprint of the impinging shock to that of the expansion wave is only $\approx 10\text{cm}$ for this ‘thickBL/Short Generator’ ($\delta_0 \approx 2.1 - 3.7\text{mm}$ upstream boundary layer) interaction, giving $L_{interaction}/\delta_0 \approx 3 - 5$, compared to that of $\delta_0/L_{interaction} \approx 21$ for the ‘thinBL/Long Generator’ Schülein case. Oddly, however, most of the flow-except the separation region- is actually well represented by the CFD results, possibly since the flow is now more dominated by inviscid features.

3 Summary

We have examined the performance of independent implementations of the SST model into two NASA CFD codes as applied to hypersonic 2D turbulent compression corner and impinging shock interactions.

A detailed examination of the sensitivity of the SST turbulence model to test parameters when applied to 2D hypersonic shock-wave/turbulent boundary layer interactions, and as implemented in the DPLR Real-Gas Navier-Stokes code, has been accomplished. The primary test condition parameters considered are those of Mach number, Reynolds number, wedge angle or shock strength. Supplemental calculations were accomplished with the Cfl3d Perfect-Gas Navier-Stokes code so as to isolate the influence of turbulence model implementation. Emphasis was placed on computations of the experimental cases of Holden’s Hypersonic Mach 8.2 compression corner, and of Settles Supersonic Mach 2.84 compression corners as each of these provide extensive variation in both Reynolds number and shock strength at two extremes of Mach number. Two additional cases of impinging hypersonic shock wave turbulent boundary layer interactions were accomplished so as to provide additional insight on the performance of the SST turbulence model relevant to scramjet

inlet design and analysis.

Supporting information upon which these detailed examinations were accomplished included engineering based correlations and non-dimensional pressure distribution transformations based on Free Interaction Theory. A discussion of Free Interaction Theory leading to a simplified algorithmic formulation for application to these present cases, as well as an update of an incipient separation correlation based on recent hypersonic data also facilitated this evaluation of the widely used SST turbulence model's ability to accurately predict separated hypersonic SWTBLI.

Overall, the primary observed deficiencies in the computed solutions were found by comparison of the CFD results with experiment and include:

1. overprediction of separation extent by SST for compression corner SWTBLI;
2. underprediction of separation bubble pressure by SST for impinging SWTBLI;
3. overprediction of post-reattachment wall heat transfer by SST for both impinging and compression corner SWTBLI;
4. overprediction of wall-heating for 'acreege' boundary layer, along with inferior post-analysis methodologies of the RANS CFD for upstream boundary layer thicknesses; and
5. loss of sensitivity to Reynolds number variations of the separation extent at high Mach numbers for the compression corner case. This contrasted with excellent tracking of Reynolds number variations of separation extent at lower Mach numbers.

The above enumerated behaviors for SWTBL interactions are unlikely to be corrected by simple changes in the SST turbulence model, as corrections in a simple eddy-viscosity model needed for each of these areas of disagreement are contradictory in their effect. It is suggested that the most promising avenue of exploration for improvement would be for incorporation of an Explicit Algebraic Reynolds Stress model, EARSm, as such a model retains the simplicity of the two-equation models, yet with the improved constitutive relation providing the full Reynolds stress tensor, the known deficiencies of two-equation eddy viscosity models in over-predicting turbulent production for reattaching/stagnation point regions and inability to incorporate known effects of the normal strain terms in separating flows can be addressed. Furthermore, it is suggested the turbulent heat transfer modeling be decoupled from turbulent momentum transfer modeling as the use of a constant turbulent Prandtl number as used with current two-equation models closely couples eddy diffusivity for heat transfer with that for momentum transfer and prohibits independent correction of the several major model deficiencies observed (too high heat transfer, but insufficient resistance to separation). Additionally, consideration of the impinging shock flow structures, specifically as the response of the separated viscous layer at the top of the recirculation region may play a significant role in the under-prediction

of separation bubble pressure, reveals the probable need for inclusion of curvature correction terms into the turbulence models applied to these flows.

For compression corner cases, the separation extent tended to be over-predicted relative to experiment, probably associated with a tendency to predict early incipient separation regardless of Mach number. DPLR/SST tends to separate too early, by about 10% or 2° - 3° in wedge angle for incipient separation for compression corners. The effect of this continues with an over-prediction of separation extent for compression corner wedge angles past incipient separation. This contrasts with CFL3D/SST which consistently agrees with experimental separation extent for all compression corner angles for the Holden Mach 8.2 cases. A similar result is observed for the Mach 3 Settles experiment, except both Cfl3d/SST and DPLR/SST tend to separate by about 2° in wedge angle too early. A change in CFL3D from thin-layer to full-NS resulted in no change in separation size, while a change in CFL3D turbulent production term from approximate (vorticity-based) to ‘exact’ strain based turbulent production led to a decrease in separation extent.

At lower Mach number, the DPLR/SST and Cfl3d/SST sensitivity to Reynolds number variation appeared to track the experiment and related correlation of Settles, however, at higher Mach number the SST results became quite insensitive to Reynolds number variation in contrast to the observed experimental tendency. The predicted separation bubble pressure was reasonably well-predicted with respect to both experiment and Free Interaction Theory, for the compression corner cases regardless of Mach number and Reynolds number.

For the impinging shock cases, two sub-types of such interactions were observed experimentally: a. ‘thin Boundary Layer/long shock generator’ case, represented by the Mach 5 Schülein experiment; and b. ‘thick Boundary Layer/short shock generator’ case, represented by the Mach 8.2 Kussoy and Horstman experiment. For the Schülein case, it was found that the expansion wave off the trailing edge of the shock generator terminated the interaction only after the interaction had become ‘fully developed’ and followed by an extended post-reattachment region of constant high pressure level. In contrast, for the Kussoy case, the expansion wave terminated the interaction soon after reattachment with the pressure rise only just reaching its’ peak value prior to the decline in pressure associated with the expansion wave.

For the Schülein case, the experimental separation bubble pressure distribution was found to conform quite well with Free Interaction theory as to shape and magnitude level. Also, the CFD/SST computed separation extent was in good agreement with the observed experimental measured extent. However, the CFD/SST computed separation bubble was only about 1/2 of the experimental level (and the level predicted by Free Interaction Theory). The DPLR/SST and Cfl3d/SST both agreed with each other as to their basic behavior on the Schülein impinging shock

experiment. Possible reasons for the observed disagreement between the numerical and experimental results are considered. It is suggested that both the influence of the inviscid solver and inadequate representation of normal stress effects contribute to the under-prediction of separation bubble pressure for the impinging shock cases.

For the Kussoy case, the experimental separation bubble proved not to agree with the Free Interaction theory, being at considerably lower pressure, likely due to the premature termination of the interaction by the expansion wave distorting the reflection/reattachment shock. An overshoot in CFD computed wall heat transfer also occurred, although not as severe as for the compression corner cases.

These observed deficiencies in RANS/SST solutions serve as a cautionary note to those attempting to rely on CFD methods directly embedded as the fluids analysis engine in MDO optimization methods. Such an approach can well prove problematic when such analysis methods are applied to hypersonic shock wave turbulent boundary layer interactions, such as in the design of vehicle control surfaces or scramjet inlets, particularly when separated off-design performance is included in the constraint list. Rather than pursuing the expense and effort of embedding complex CFD methods with unvalidated or inaccurate parametric response into MDO optimization procedures, a more effective analysis engine for MDO methods may prove to be an intermediate analysis step providing either interpolation, a neural net or an Engineering-based method making extensive use of engineering correlations (e.g. see Garcia [1] and related citations), and which are best calibrated by a combination of vetted experiments and sparse CFD solutions. A further cautionary note must be made by the appearance of what appears to be a form of ‘digital noise’ for separated SWTBL cases at hypersonic conditions, and may degrade the performance of MDO design procedures, particularly if MDO algorithms based on numerical differentiation are employed.

As a final observation, it is clear that over the past 45-50 years, since the experiments of Settles and of Holden, there has simply been too few quality 2D hypersonic/supersonic compression corner experiments providing both a range of shock strength and Reynolds number variation at a variety of Mach numbers. Well-designed hypersonic experiments are indeed expensive, so to maximize their benefit parametric variation about nominal test conditions can lend substantial added value at reasonable economic cost. Along with the absence of new experiments, there is too much scatter to provide adequate confidence in correlations in the hypersonic regime. In the design of new experiments, it is hoped that this present study can demonstrate the value of such data obtained at little additional cost/effort by varying the Reynolds number. The addition of even this extra dimension of parametric variation in hypersonic experiment design can considerably enhance the utility of such data in understanding the ability of predictive methods to correctly model general trends as needed for optimization procedures.

References

1. Garcia, J. A., Brown, J. L., Kinney, D. J., Bowles, J. V., Huynh, L. C., Jiang, X. J., Lau, E. and Dupzyk, I. C., "Co-Optimization of Mid-Lift/Drag Vehicle Concepts for Mars Atmospheric Entry," AIAA Paper 2010-5052, 10th AIAA/ASME Joint Thermophysics and Heat Transfer Conference, Chicago, Illinois, 28 Jun-1 July, 2010.
2. Brown, J. L., "Shock Wave Impingement on Boundary Layers at Hypersonic Speeds: Computational Analysis and Uncertainty," AIAA Paper 2011-3143, 42nd AIAA Thermophysics Conference, Honolulu, Hawaii, 27-30 Jun, 2011.
3. Brown, J. L., "Hypersonic Shock Wave Impingement on Turbulent Boundary Layers: Computational Analysis and Uncertainty," *J. Spacecraft and Rockets*, Vol. 50, No. 1, Jan-Feb 2013.
4. Marvin, J. G, Brown, J. L. and Gnoffo, P. A., "Experimental Database with Baseline CFD Solutions: 2-D and Axisymmetric Hypersonic Shock-Wave Turbulent Boundary Layer Interactions," NASA TM 2013-216604, Nov. 2013.
5. Brown, J. L., "Turbulence Model Validation for Hypersonic Flows," AIAA Paper 2002-3143, 8th AIAA/ASME Joint Thermophysics and Heat Transfer Conference, St. Louis, Missouri, 24-26 Jun, 2002.
6. Settles, G. S. and Dodson, L. J., "Hypersonic Shock/Boundary-Layer Interaction Database," NASA CR 177577, April 1991.
7. Settles, G. S. and Dodson, L. J., "Hypersonic Turbulent Boundary-Layer and Free-Shear Layer Database," NASA CR 177610, April 1993.
8. Settles, G. S. and Dodson, L. J., "Hypersonic Shock/Boundary-Layer Interaction Database: New and Corrected Data," NASA CR 177638, April 1994.
9. Settles, G. S. and Dodson, L. J., "Supersonic and Hypersonic Shock/Boundary-Layer Interaction Database," *AIAA Journal*, Vol. 32, No. 7, July 1994, pp. 1377-1383.
10. Settles, G. S., Bogdonoff, S. M. and Vas, I. E., "Incipient Separation of a Supersonic Turbulent Boundary Layer at Moderate to High Reynolds Number," AIAA Paper 1975-7, AIAA 13th Aerospace Sciences Meeting, Pasadena, CA, Jan 20-22, 1975.
11. Settles, G. S., Fitzpatrick, T. J. and Bogdonoff, S. M., "Detailed study of Attached and Separated Compression Corner Flowfields in High Reynolds number Supersonic Flow," *AIAA Journal*, Vol. 17, No. 6, 1979, pp.579-585.

12. Settles, G. S., Gilbert, R. B. and Bogdonoff, S. M., "Data Compilation For Shock Wave/Turbulent Boundary Layer Interaction Experiments On Two-Dimensional Compression Corners," *Princeton University Report 1489-MAE*, Princeton Univ., 1980.
13. Wilcox, D. C., "Turbulence Modeling for CFD," 3rd Edition, DCW Industries, Inc., La Canada, CA, Nov. 2006.
14. Wright, M. J., Candler, G. V. and Bose, D., "Data-Parallel Line Relaxation Method for the Navier-Stokes Equations," *AIAA Journal*, Vol. 36, No. 9, 1998, pp. 1603-1609.
15. Wright, M. J., White, T. and Mangini, N., "Data Parallel Line Relaxation Code User Manual, Acadia-Version 4.01.1," NASA TM-2009-215388, Oct. 2009.
16. Rumsey, C., Biedron, R. and Thomas, J., "CFL3D: Its History and Some Recent Applications," NASA TM-112861, May 1997.
17. Bose, D., Brown, J. L., Prabhu, D. K., Gnoffo, P., Johnston, C. J. and Hollis, B., "Uncertainty Assessment of Hypersonics Aerothermodynamic Prediction Capability," AIAA Paper 2011-3141, 42nd AIAA Thermophysics Conference, Honolulu, Hawaii, 27-30 Jun, 2011.
18. Bose, D., Brown, J. L., Prabhu, D. K., Gnoffo, P., Johnston, C. J. and Hollis, B., "Uncertainty Assessment of Hypersonics Aerothermodynamic Prediction Capability," *J. Spacecraft and Rockets*, Vol. 50, No. 1, Jan-Feb 2013.
19. Gnoffo, P. A., Berry, S. A. and Van Norman, J. W., "Uncertainty Assessments in Simulations of 2D and Axisymmetric Hypersonic Shock Wave-Turbulent Boundary Layer Interactions at Compression Corners," AIAA Paper 2011-3143, June 27-30, Honolulu, HI, 2011.
20. Gnoffo, P. A., Berry, S. A. and Van Norman, J. W., "Uncertainty Assessments in Simulations of 2D and Axisymmetric Hypersonic Shock Wave-Turbulent Boundary Layer Interactions at Compression Corners," *J. Spacecraft and Rockets*, Vol. 50, No. 1, Jan-Feb 2013.
21. Ames Research Staff, "Equations, Tables, and Charts for Compressible Flow," NACA Rept. 1135, 1953.
22. Wolf, T., "Comment on Approximate Formulation of Weak Oblique Shock Wave Angle," *AIAA Journal*, Vol. 31, No. 7, 1993, p. 1363.
23. Chapman, D. R., Kuehn, D. M. and Larson, H. K., "Investigation of Separated Flows in Supersonic and Subsonic Streams with Emphasis on the Effect of Transition," NACA Report 1356, 1958.

24. Reshotko, E. and Tucker, M., "Effect of a discontinuity on Turbulent Boundary-Layer-Thickness Parameters with Application to Shock-Induced Separation," NACA TN-3454, May 1955.
25. Erdos, J. and Pallone, A., "Shock-boundary layer interaction and flow separation," in: Proc. Heat Transfer and Fluid Mechanics Inst., Stanford Univ Press, 1962.
26. Lewis, J. E., Kubota, T. and Lees, L., "Experimental Investigation of Supersonic Laminar, Two-Dimensional Boundary Layer Separation in a Compression Corner With and Without Cooling," *AIAA Journal*, Vol. 6, No. 1, 1968. p. 7-14.
27. Carriere, P., Sirieix, M. and Solignac, J. L., "Similarity Properties of the laminar or turbulent separation phenomena in a non-uniform supersonic flow," *Applied Mechanics*, International Union of Theoretical and Applied Mechanics, 1969, p 145-157.
28. Kuehn, D. M., "Turbulent Boundary-Layer Separation induced by Flares on Cylinders at Zero Angle of Attack," NASA Technical Report R-117, 1961.
29. Delery, J. and Marvin, J. G., "Shock-Wave Boundary Layer Interactions," AGARDograph AG-280, NATO, Ed. by Reshotko, E., 1986.
30. Back, L. H. and Cuffel, R. F., "Changes in Heat Transfer from Turbulent Boundary Layers Interacting with Shock Waves and Expansion Waves," *AIAA Journal*, Vol. 8, No. 10, 1970, pp. 1871-1873.
31. Holden, Michael S., "Shock Wave-Turbulent Boundary Layer Interaction in Supersonic Flow," AIAA Paper 1977-45, AIAA 15th Aerospace Sciences Meeting, Los Angeles, CA, Jan 1977.
32. Holden, M., MacLean, M., Wadhams, T. and Mundy, E., "Experimental Studies of Shock Wave/Turbulent Boundary Layer Interaction in High Reynolds Number Supersonic and Hypersonic Flow to Evaluate the Performance of CFD Codes," AIAA Paper 2010-4468, 40th Fluid Dynamics Conference and Exhibit, Chicago, Illinois, Jun 2010.
33. Menter, F. R., "Improved Two-Equation $K-\omega$ Turbulence Models for Aerodynamic Flows," NASA TM 103975, Oct. 1992.
34. Menter, F. R., "Two-Equation Eddy Viscosity Turbulence Models for Engineering Applications," *AIAA Journal*, Vol. 32, No. 8, Aug 1994, pp. 1598-1605.
35. Menter, F. R. and Esch, T., "Elements of Industrial Heat Transfer Predictions," *16th Brazilian Congress of Mechanical Engineering (COBEM)*, Uberlandia, Brazil, Nov. 2001.

36. Menter, F. R., Kuntz, M. and Langtry, R., "Ten Years of Industrial Experience with the SST Turbulence Model," in *Turbulence, Heat & Mass Transfer*, Vol. 4, Ed. by Hanjalic, K., Nagano, Y. and Tummers, M., 2003, pp. 625-632.
37. Korkegi, R. H., "Comparison of Shock-Induced Two- and Three-Dimensional Incipient Separation," *AIAA Journal*, Vol. 13, No. 4, April 1975.
38. Needham, D. A. and Stollery, J. L., "Boundary Layer Separation in Hypersonic Flow," AIAA Paper 1966-455, AIAA 4th Aerospace Sciences Meeting, Los Angeles, CA, June, 1966.
39. Babinsky, H. and Edwards, J. A., "On The Incipient Separation Of A Turbulent Hypersonic Boundary Layer," *The Aeronautical Journal*, June, 1996.
40. Roy, C. J. and Blottner, F. G., "Review and Assessment of Turbulence Models for Hypersonic Flows," AIAA Paper 2006-713, 2006.
41. Sommer, T. P., So, R. M. C. and Zhang, H. S., "Near-Wall Variable-Prandtl-Number Turbulence Model for Compressible Flows," *AIAA Journal*, Vol. 31, No. 1, Jan. 1993.
42. Xiao, X., Edwards, J. R. and Hassan, H. A., "Role of Turbulent Prandtl Number on Heat Flux at Hypersonic Mach Numbers," AIAA Paper 2005-1098, 43rd AIAA Aerospace Sciences Meeting and Exhibit, Reno, Nevada, 10-13 Jan, 2005.
43. Xiao, X., Hassan, H. A., Edwards, J. R. and Gaffney, R. L., Jr., "Role of Turbulent Prandtl Number on Heat Flux at Hypersonic Mach Numbers," *AIAA Journal*, Vol. 45, No. 4, Apr. 2007. pp 806-813.
44. Schülein, E., Krogmann, P. and Stanewsky, E., "Documentation of Two-Dimensional Impinging Shock/Turbulent Boundary Layer Interaction Flow," DLR, German Aerospace Center, Rept. IB 223-96 A 49, Göttingen, Germany, Oct, 1996.
45. Schülein, E., "Skin-Friction and Heat Flux Measurements in Shock/Boundary-Layer Interaction Flows," *AIAA Journal*, Vol. 44, No. 8, Aug 2006, pp. 1732-1741, also AIAA Paper 2004-2115, 2004.
46. Fedorova, N. N., Fedorchenko, I. A. and Schülein, E., "Experimental and Numerical Study of Oblique Shock Wave/Turbulent Boundary Layer Interaction at $M = 5$," *Computational Fluid Dynamics Journal*, Vol. 10, No. 3, Special Issue, 2001, pp. 390-395.
47. Fedorova, N. N. and Fedorchenko, I. A., "Computations of Interaction of an Incident Oblique Shock Wave with a Turbulent Boundary

- Layer on a Flat Plate,” *Journal of Applied Mechanics and Technical Physics*, Vol. 45, No. 3, 2004, pp. 358-366.
48. Kussoy, M. I. and Horstman, K. C., “Documentation of Two- and Three-Dimensional Shock-Wave/Turbulent Boundary-Layer Interaction Flows at Mach 8.2,” NASA TM 103838, May 1991.
 49. Cebeci, T. and Smith, A. M. O., “*Analysis of Turbulent Boundary Layers*,” Series in Applied Mathematics and Mechanics, Vol. XV, Academic Press, Orlando, FL, 1974.
 50. Zhang, C., Xu, J., Gao, L. and Gao, G., “Studies of Compression Corner Flowfields Using THREE Turbulent Models” *Procedia Engineering*, Vol. 31, International Conference on Advances in Computational Modeling and Simulation, 2012, p. 762-768.
 51. Steelant, J., “Effect of a Compressibility Correction on Different Turbulence Models,” *Engineering Turbulence Modelling and Experiments-5*, Ed. Rodi, W. and Fueyo, N., Elsevier Science, Ltd., 2002. pp 207-216.
 52. Kovar, A., Hannemann, S. Karl and Schülein, E., “About the Assessment of Heat Flux and Skin Friction of the DLR-TAU-code for Turbulent Supersonic Flows,” ODAS, ONERA-DLR Aerospace Symposium, 2007.
 53. Simpson, R. L., “Two-Dimensional Turbulent Separated Flows,” AGARDograph AG-278, Vol. 1, NATO, Ed. by Young, A. D., 1985.
 54. Wallin, S. and Johansson, A. V., “An explicit algebraic Reynolds stress model for incompressible and compressible turbulent flows,” *Journal of Fluid Mechanics*, Vol. 403, p. 89-132, Jan. 2000.
 55. Hellsten, A. and Laine, S., “Explicit Algebraic Reynolds-Stress Modelling in Decelerating and Separating Flows,” AIAA Paper 2000-2313, June 2000.
 56. Hellsten, A., “New Advanced $k - \omega$ Turbulence model for High-Lift Aerodynamics,” *AIAA Journal*, Vol. 43, No. 9, 2005.

3.1 Tables

Experiment	Type	Mach No	ReU $10^6/m$	L, m	ShockGenAngle
	Wedge				
Settles	2D	2.84	67.16	1.98	8, 16, 20, 24 $^\circ$
A2.Holden	2D	8.2	143.74	0.99568	27, 30, 33, 36 $^\circ$
A2.Holden	2D	11.3	36.51	1.02362	36 $^\circ$
A5.Kussoy	Axi	7.05	5.8	1.39	20, 30, 32.5, 35 $^\circ$
A6.Williams	Axi	8.98	50.3	0.72	36 $^\circ$
	Impinging				
B1.Schülein	2D	5.0	38.8	0.35	6, 10, 14 $^\circ$
B2.Murray	Axi	8.99	40.34	0.76	4.7, 10 $^\circ$
B3.Kussoy	2D	8.2	4.91	1.6	5, 8, 9, 10, 11 $^\circ$
B4.Holden	2D	11.4	36.51	0.88392	20 $^\circ$

Table 1. Hypersonic 2D or Axisymmetric SWTBLI Cases. Experimental cases are given in terms of Ref [4] where applicable. Note Settles experiment was run on a wind tunnel wall, so run length given is from nozzle to wedge.

Experiment	M_e	Gas	P_T , MPa	T_0^o , K	T_{aw}^o , K	T_{wall}^o , K
Settles	2.84	Air	0.68	262	244.2	276
A2.Holden	8.2	Air	116.8	1025.8	920.78	296
A2.Holden	11.3	Air	139.0	1619	1447.6	300
A5.Kussoy	7.05	Air	2.495	888.38	799.58	311
A6.Williams	8.98	N_2	60.8	1150	1031	293
B1.Schülein	5.0	Air	2.2351	410.35	376.264	300
B2.Murray	8.99	N_2	60.8	1150	1031	293
B3.Kussoy	8.2	Air	24.95	888.38	799.58	300
B4.Holden	11.4	Air	164.6	1700.5	1520.4	300

Table 2. Total or Stagnation Conditions for SWTBLI Cases.

Experiment	M_e	U_∞ , m/s	p_e , kPa	ρ_e , kg/m ³	T_e^o , K	μ_∞ , kg/m-s
Settles	2.84	570	23.6	0.82014	100.3	7.002 10 ⁻⁶
A2.Holden	8.2	1385	10.188	0.50	71	4.989 10 ⁻⁶
A2.Holden	11.3	1769	1.4437	0.082455	61	4.285 10 ⁻⁶
A5.Kussoy	7.05	1274	0.576	0.0252	81.2	5.700 10 ⁻⁶
A6.Williams	8.98	1500	2.926	0.1467	67.16	4.724 10 ⁻⁶
B1.Schülein	5.0	828.4	4.304	0.21815	68.73	4.830 10 ⁻⁶
B2.Murray	8.99	1500	2.898	0.1457	66.97	4.710 10 ⁻⁶
B3.Kussoy	8.2	1446	0.430	0.0187	81.0	5.686 10 ⁻⁶
B4.Holden	11.4	1814	1.611	0.08910	63	4.426 10 ⁻⁶

Table 3. Upstream Boundary Layer properties for SWTBLI Cases. Keyes Relation for either dry Air or N2 is used for dynamic viscosity.

Experiment	M_e	τ_0 , Pa	Q_0 , W/cm ²	δ_0 , mm	δ_0^* , mm	θ_0 , mm	H
Settles	2.84	145.0	-0.946	23.72	6.00	1.15	5.21
A2.Holden	8.2	278.3	14.87	13.3	6.30	0.34	18.17
A2.Holden	11.3	69.28	5.32	21.052	10.506	0.341	30.77
A5.Kussoy	7.05	21.82	0.9887	30.0352	13.647	0.920	14.84
A6.Williams	8.98	113.7	6.8115	13.5289	6.631	0.318	20.83
B1.Schülein	5.0	73.48	0.7505	4.813	2.000	0.202	10.94
B2.Murray	8.99	112.046	6.7087	14.028	6.962	0.333	20.87
B3.Kussoy	8.2	18.82	1.128	39.5528	17.6655	0.9868	17.90
B4.Holden	11.4	78.832	6.29	18.715	9.386	0.303	30.97

Table 4. Upstream Boundary Layer properties for SWTBLI Cases, from Wilcox EddyBL/Cebeci-Smith Turbulence Model.

Experiment	M_1	α_{wedge}^o	θ_{shock}^o	M_2	p_2/p_1	T_2/T_1
Settles	2.84	8.	26.822	2.466	1.7492	1.179
		16.	34.571	2.088	2.8631	1.396
		20.	39.116	1.888	3.5788	1.525
A2.Holden	8.2	24.	44.260	1.676	4.4168	1.673
		27.	35.184	2.947	25.8785	5.279
		30.	39.145	2.597	31.0957	6.150
		33.	43.313	2.277	36.7477	7.092
		36.	47.783	1.976	42.8612	8.112
A2.Holden	11.3	36.	46.783	2.096	78.952	14.129
B1.Schülein	5.0	6.0	15.875 : 17.481	4.395 : 3.899	3.762	1.485
		10.0	19.376 : 22.237	4.000 : 3.285	7.626	1.899
		14.0	23.287 : 27.686	3.603 : 2.736	13.624	2.402
B3.Kussoy	8.2	5.0	10.681 : 11.811	7.012 : 6.116	5.655	1.704
		8.0	13.408 : 15.277	6.316 : 5.131	12.418	2.306
		9.0	14.384 : 16.516	6.087 : 4.838	15.552	2.543
		10.0	15.388 : 17.793	5.861 : 4.561	19.155	2.799
		11.0	16.417 : 19.107	5.639 : 4.301	23.232	3.074
B4.Holden	11.4	20.0	25.480 : 31.309	4.363 : 2.746	162.616	10.764

Table 5. Shock Strength for 2D Planar SWTBLI Cases, from NACA 1135, Ref [21] and Wolf, [22]. Impinging shock 2D case values are for the inviscid 2-shock impinging/reflection shock problem; Hence, 2 shock angles and Mach numbers are given, while the pressure and temperature ratios are for the effect of the two shocks combined.

Experiment	M_1	$p_{w,0}$ Pa	$\tau_{w,o}$, Pa	q_0 , kPa	δ_0^* , mm
Settles	2.84	23600.0	145.00	133.244	6.000
A2.Holden	8.2	10188	278.3	479.529	6.299
A2.Holden	11.3	1443.7	69.28	129.042	10.507
A5.Kussoy	7.05	576.0	21.82	20.040	13.647
A6.Williams	8.98	2926.0	113.7	165.168	6.631
B1.Schülein	4.984	4304.0	73.48	74.838	2.730
B2.Murray	8.98	2898.0	112.046	163.587	6.962
B3.Kussoy	8.2	430.0	18.82	20.239	17.665
B4.Holden	11.4	1611.016	78.832	146.557	9.386

Table 6. Free Interaction Transformation Variables for SWTBLI Cases.

Experiment	M_1	A_ξ , Pa	B_ξ	$p_{w,s}$, kPa	$p_{w,b}$, kPa
Settles	2.84	3812.72	18.59	39.689	46.476
A2.Holden	8.2	5726.62	14.55	34.354	44.548
A2.Holden	11.3	1260.37	12.86	6.762	9.006
A5.Kussoy	7.05	354.00	11.47	2.0690	2.700
A6.Williams	8.98	2051.51	12.76	11.584	15.235
B1.Schülein	5.0	1500.84	14.44	10.637	13.309
B2.Murray	8.99	2026.76	12.79	11.450	15.059
B3.Kussoy	8.2	304.66	11.45	1.715	2.257
B4.Holden	11.4	1426.45	12.79	7.630	10.170

Table 7. Free Interaction Variables for SWTBLI Cases.

$p_{w,s}$ and $p_{w,b}$ correspond to $\mathcal{P}_\xi = 4.22$, and 6.0, respectively; where, $\mathcal{P}_\xi = (P_w - P_0)/A_\xi$, and $\xi = (X - X_0)/(\kappa_\xi B_\xi \delta_0^*)$.

3.2 Figures

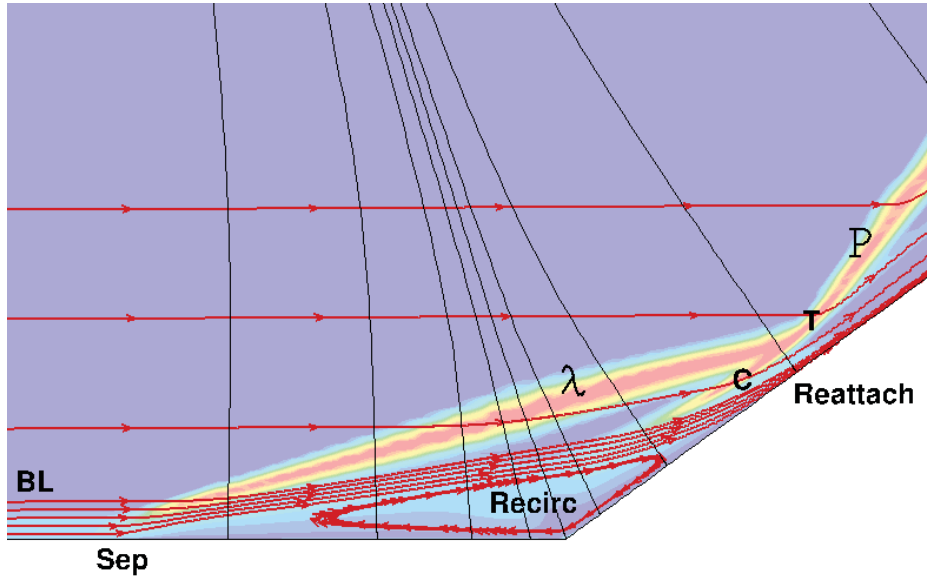


Figure 1. Hypersonic Compression Corner Separated Shock Boundary Layer Topology: Holden $M_\infty = 8.2$, 36° case. BL-upstream boundary layer, P -Primary Shock System, C -compression or reattachment shock, λ -separation shock.

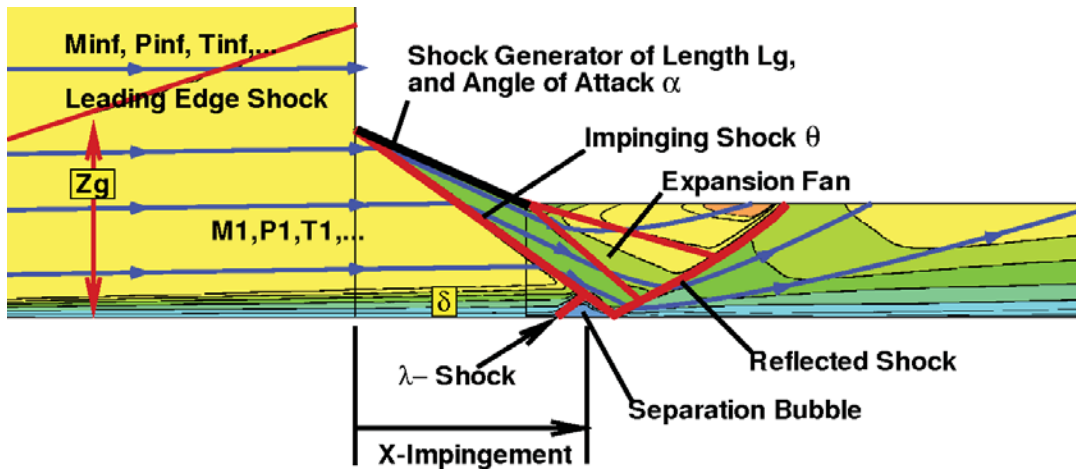


Figure 2. Hypersonic Impinging Shock-Wave/Boundary-Layer Flow Topology: Schülein Mach 5, 14° case.

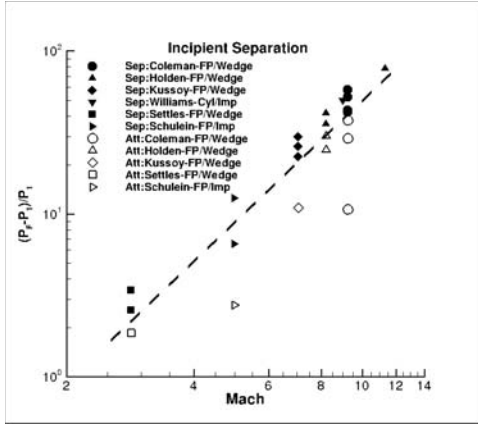


Figure 3. Incipient Separation: Dependence on Mach Number.

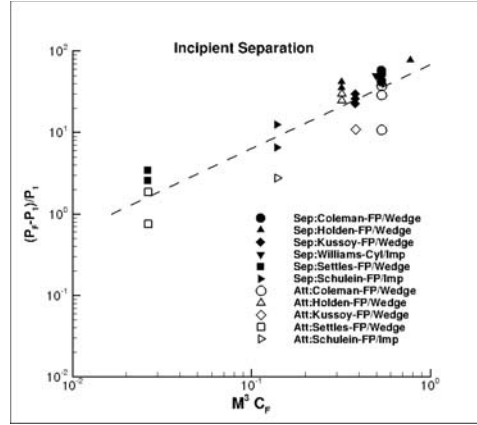


Figure 4. Incipient Separation: Dependence on $M^3 C_F$.

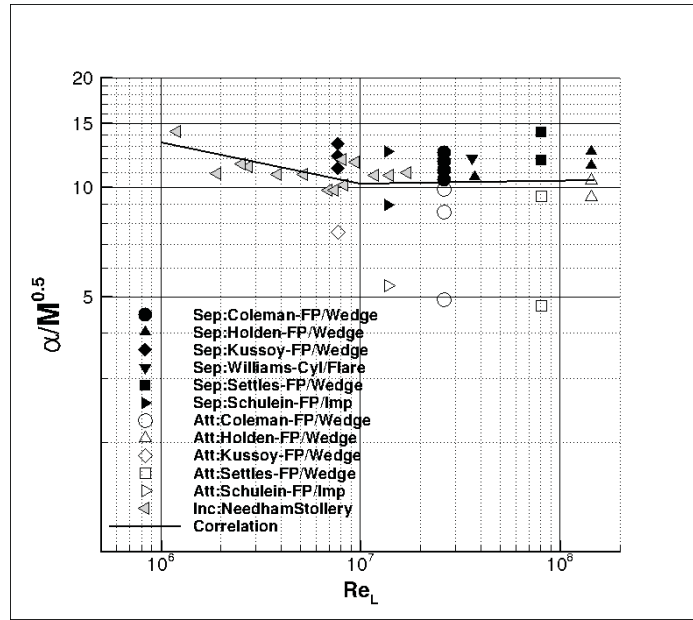


Figure 5. Incipient Separation: Dependence of Wedge Angle on Mach and Reynolds Number. Updated Correlation.

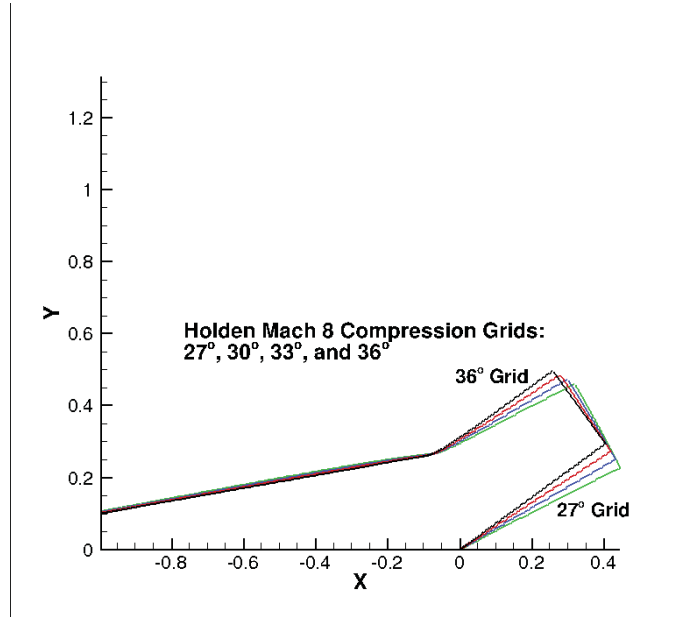


Figure 6. Holden Mach 8 Compression Corner Grids: 27°, 30°, 33° and 36° Wedge Angle.

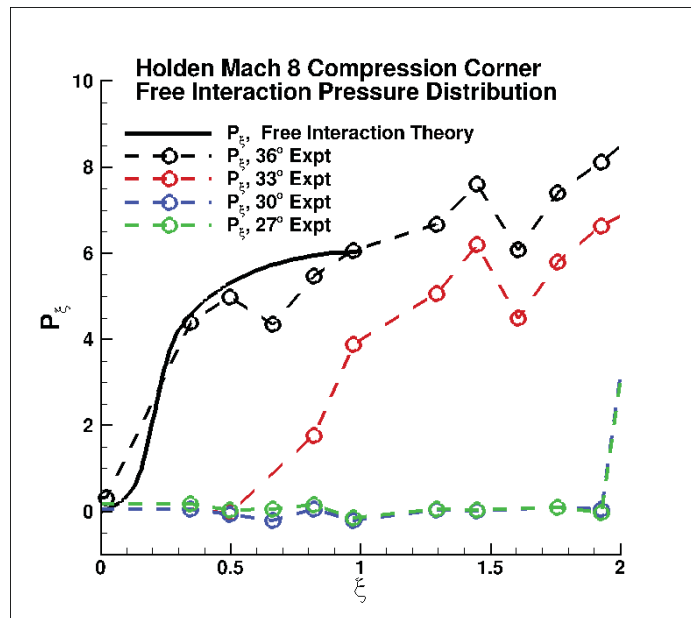


Figure 7. Holden Mach 8 Separation Region Wall Pressure Distribution, Free Interaction Variables: 27°, 30°, 33° and 36° Wedge Angle.

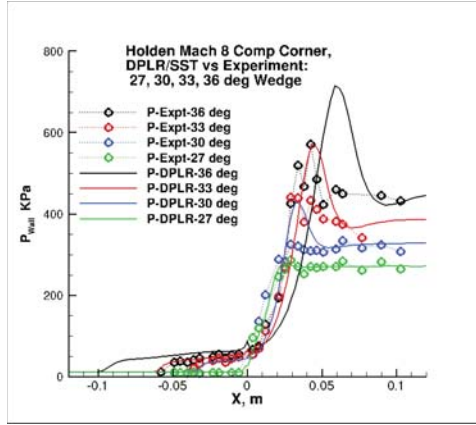


Figure 8. Holden $M_\infty = 8.2$ SWBLI, P_{Wall} vs X , DPLR/SST vs Expt.

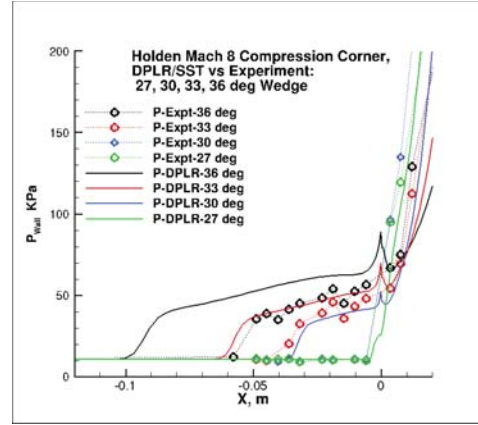


Figure 9. Holden $M_\infty = 8.2$ SWBLI, P_{Wall} vs X , DPLR/SST vs Expt, Expanded.

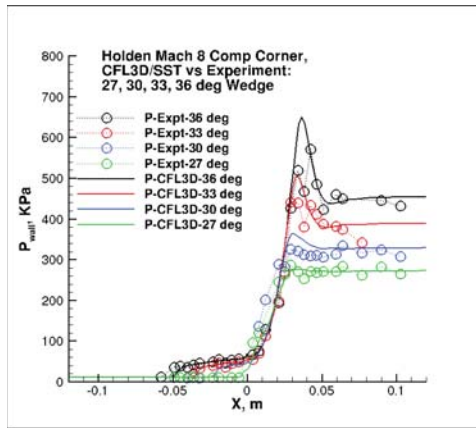


Figure 10. Holden $M_\infty = 8.2$ SWBLI, P_{Wall} vs X , CFL3D/SST vs Expt.

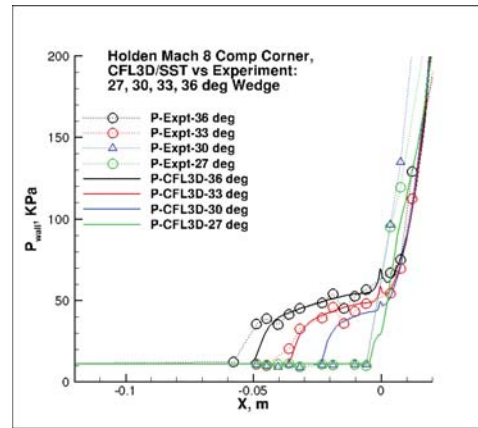


Figure 11. Holden $M_\infty = 8.2$ SWBLI, P_{Wall} vs X , CFL3D/SST vs Expt, Expanded.

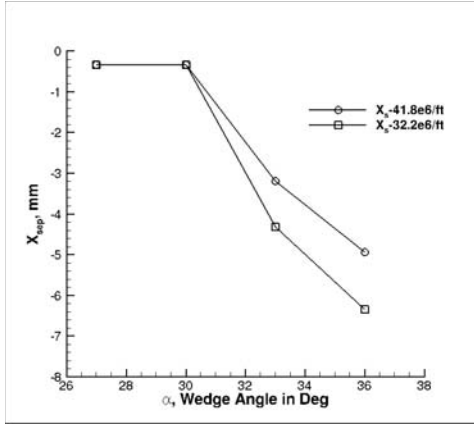


Figure 12. Holden $M_\infty = 8.2$ Separation Extent Dependence on Wedge Angle.

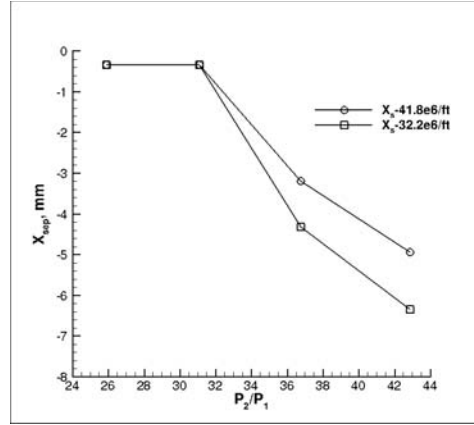


Figure 13. Holden $M_\infty = 8.2$ Separation Extent Dependence on Primary Shock Strength.

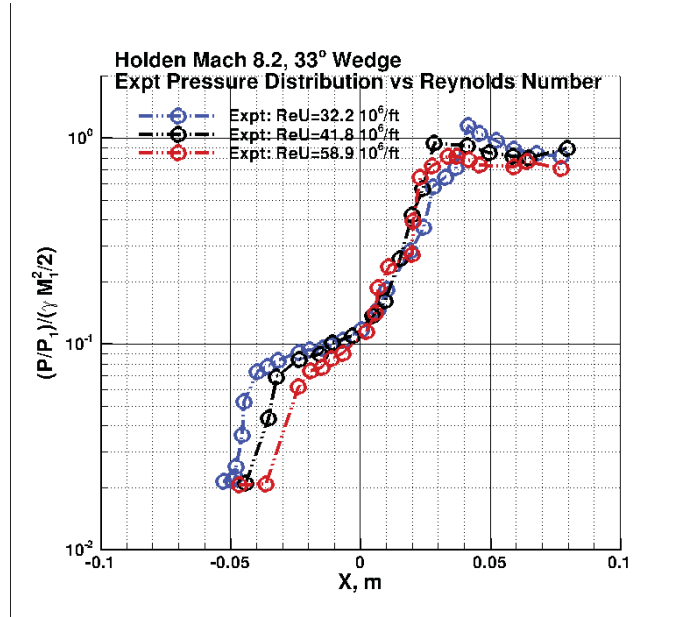


Figure 14. Holden $M_\infty = 8.2$, 33° Wedge: Experimental Wall Pressure Distribution Dependence on Reynolds Number.

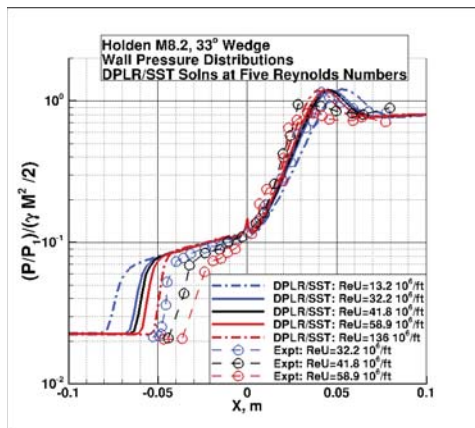


Figure 15. Holden $M_\infty = 8.2$, 33° Wedge: Wall Pressure Distribution Dependence on Reynolds Number for DPLR/SST Solns.

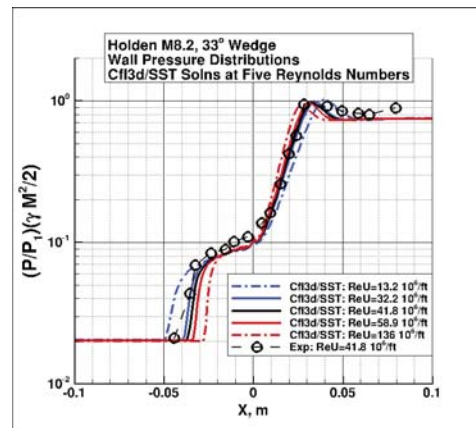


Figure 16. Holden Mach 8, 33° Wedge: Wall Pressure Distribution Dependence on Reynolds Number for CFL3D/SST Solns.

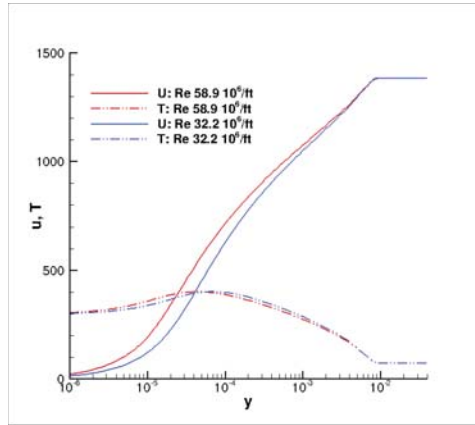


Figure 17. Holden $M_\infty = 8.2$, 33° Wedge: Upstream Velocity and Temperature Profiles from DPLR/SST Solutions, Reynolds number dependence.

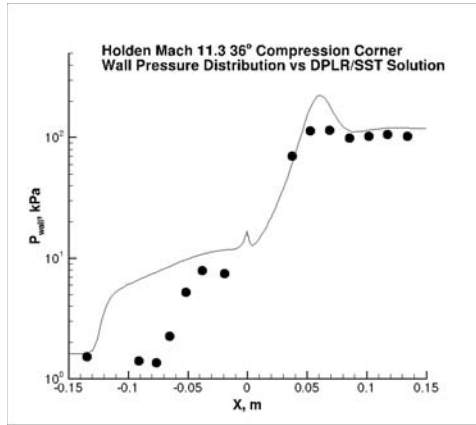


Figure 18. Holden $M_\infty = 11.3$, 36° Compression Corner Wall Pressure Distribution. Expt vs DPLR/SST Solutions.

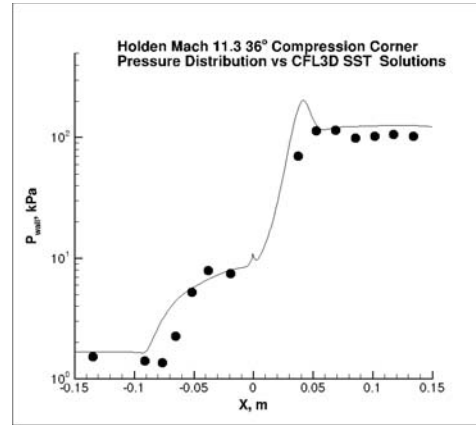


Figure 19. Holden $M_\infty = 11.3$, 36° Compression Corner Wall Pressure Distribution. Expt vs CFL3D/SST Solutions.

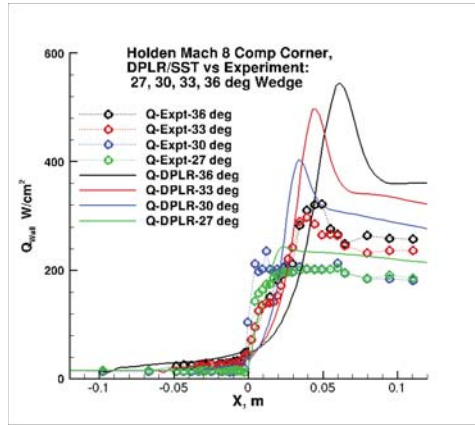


Figure 20. Holden $M_\infty = 8.2$ SWBLI, Wall Heat Transfer vs X, DPLR/SST vs Expt.

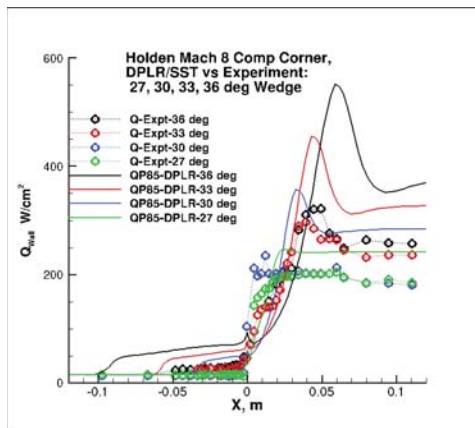


Figure 21. Holden $M_\infty = 8.2$ SWBLI, Wall Heat Transfer vs X, QP85 DPLR/SST vs Q Expt.

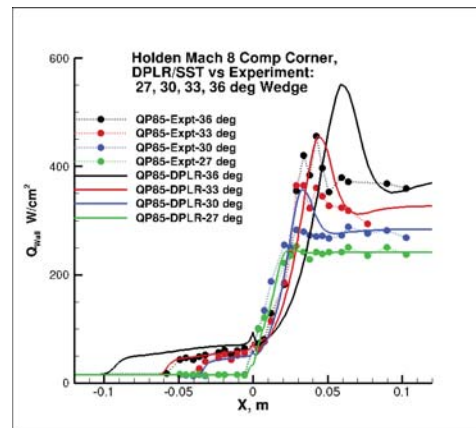


Figure 22. Holden $M_\infty = 8.2$ SWBLI, Wall Heat Transfer vs X, QP85 DPLR/SST vs QP85 Expt.

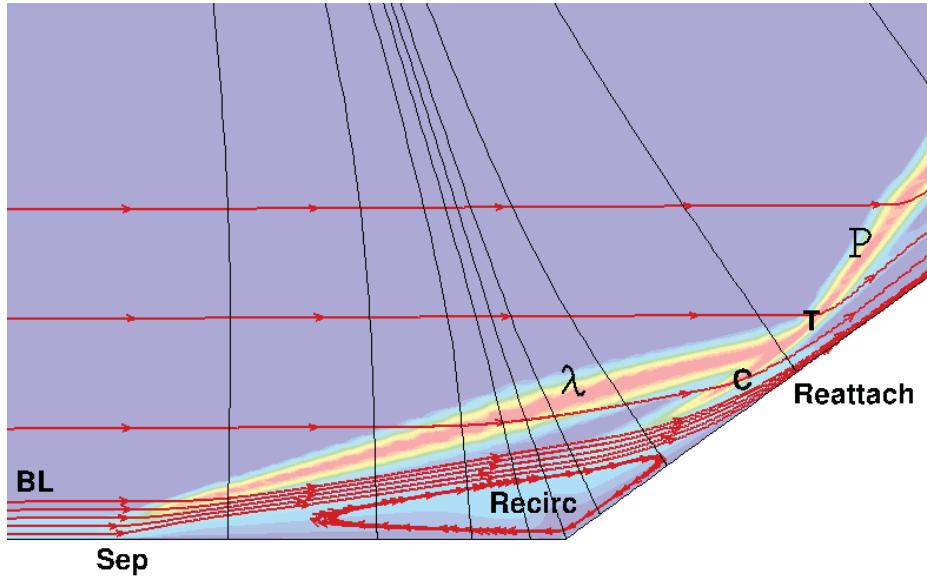


Figure 23. Holden $M_\infty = 8.2$ Separated Shock Boundary Layer Topology and Streamlines, 36° Wedge Angle. DPLR/SST solution.

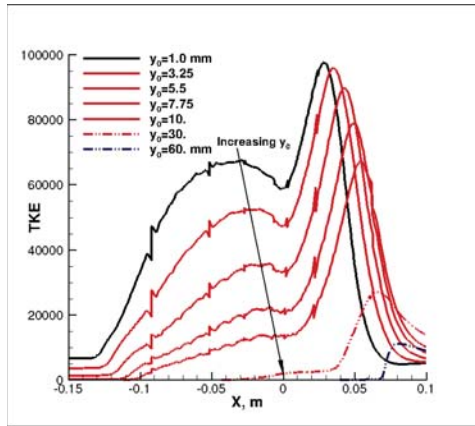


Figure 24. Development of SST Turbulent Kinetic Energy along Boundary Layer Streamlines through the Separation and Reattachment regions for the Holden $M_\infty = 8.2$ 36° Wedge Angle SWBLI.

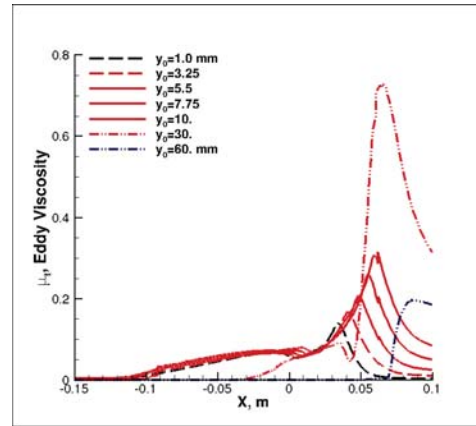


Figure 25. Development of SST Eddy Viscosity along Boundary Layer Streamlines through the Separation and Reattachment regions for the Holden $M_\infty = 8.2$ 36° Wedge Angle SWBLI.

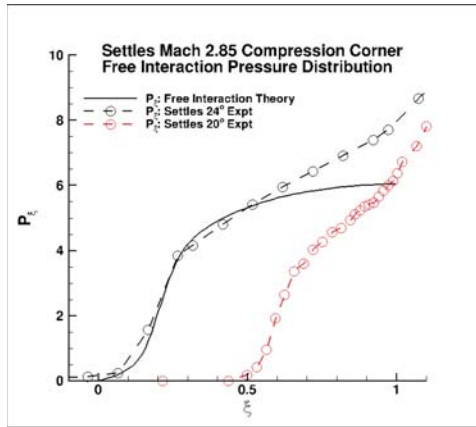


Figure 26. Settles $M_\infty = 2.85$ Compression Corner Separation Wall Pressure Distribution, Free Interaction Variables: 20° and 24° Cases.

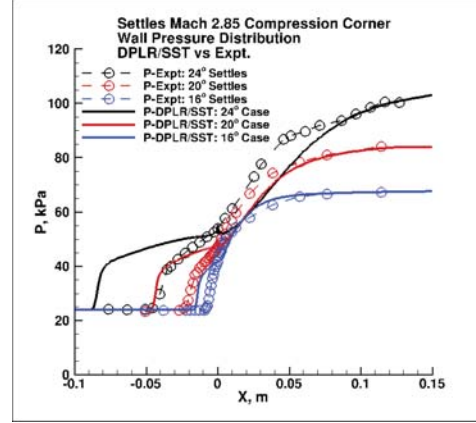


Figure 27. Settles Compression Corner Experimental vs DPLR/SST Wall Pressure Distribution, $M_\infty = 2.85$: 16° , 20° and 24° Cases.

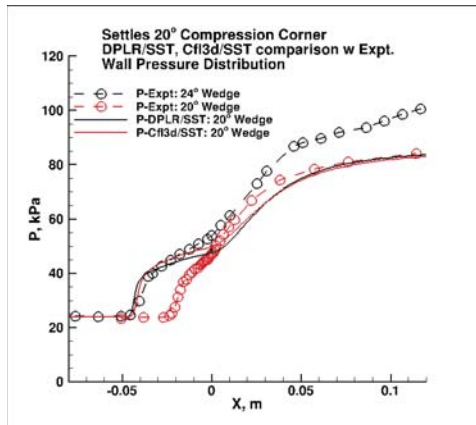


Figure 28. Settles Compression Corner Wall Pressure Distribution, $M_\infty = 2.85$: DPLR/SST and CFL3D/SST comparison with Experiment, 20° Case.

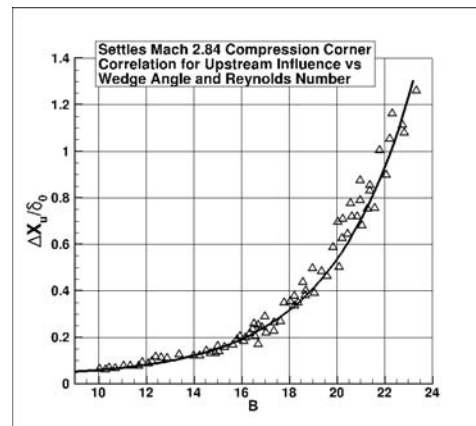


Figure 29. Settles Correlation for Upstream Influence Dependence on Reynolds Number and Wedge Angle for Turbulent Compression Corner Wall Pressure Distribution, $M_\infty = 2.85$. Settles Data are open symbols, Settles Correlation is solid line, Extracted from Ref [10].

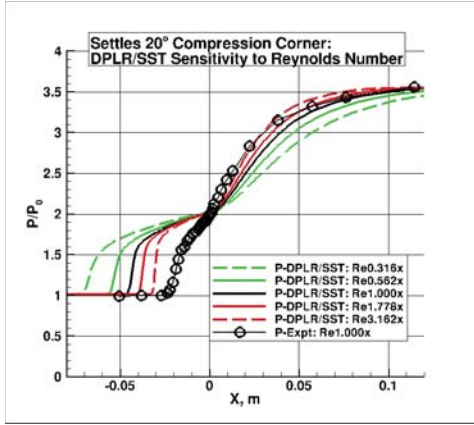


Figure 30. Settles Compression Corner Wall Pressure Distribution, $M_\infty = 2.85$, 20° Case: DPLR/SST Reynolds Number Sensitivity of Separation Extent.

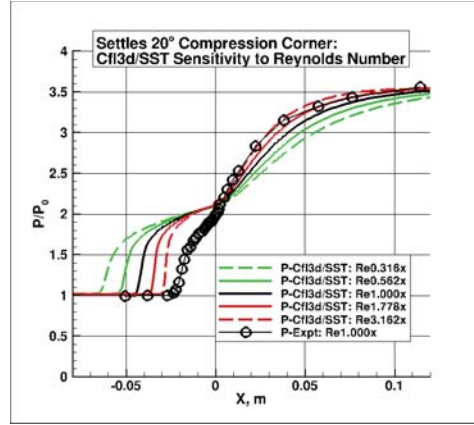


Figure 31. Settles Compression Corner Wall Pressure Distribution, $M_\infty = 2.85$, 20° Case: Cf13d/SST Reynolds Number Sensitivity of Separation Extent.

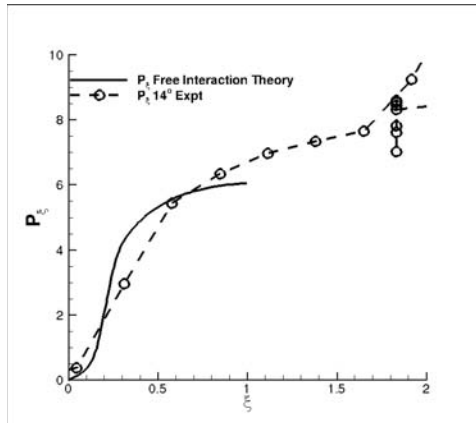


Figure 32. Schülein $M_\infty = 5$ Impinging Shock Separation Region Wall Pressure Distribution, Free Interaction Variables: 14° Case.

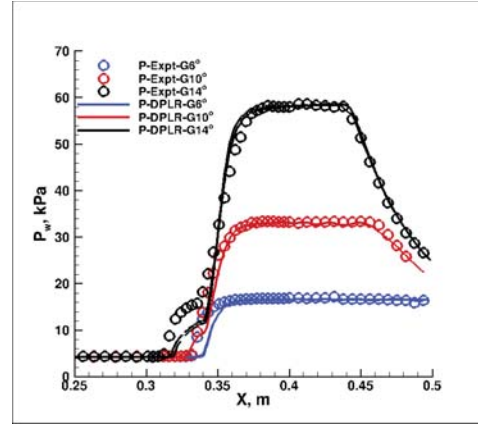


Figure 33. Schülein $M_\infty = 5$ Impinging SWTBL Interaction Experimental Wall Pressure Distribution: 6° , 10° and 14° Shock Generator Cases.

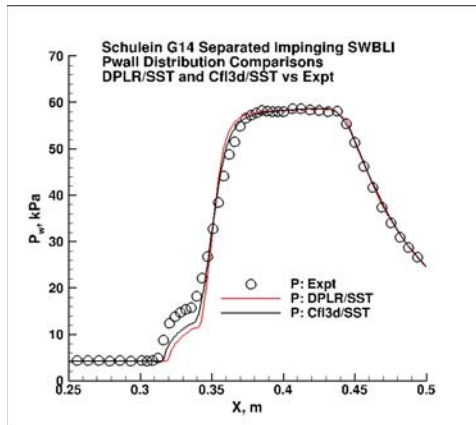


Figure 34. Schülein $M_\infty = 5$ Impinging Shock Separation Region Wall Pressure Distribution, DPLR/SST comparison with CFL3D/SST: 14° Shock Generator.

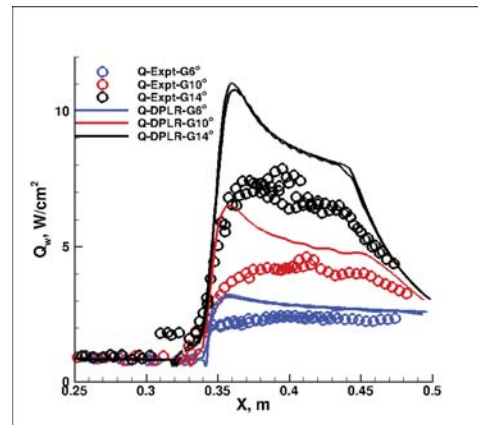


Figure 35. Schülein $M_\infty = 5$ Impinging SWTBL Interaction Wall Heat Transfer Distribution, DPLR/SST vs Experimental Measurements: 6° , 10° and 14° Shock Generator Cases.

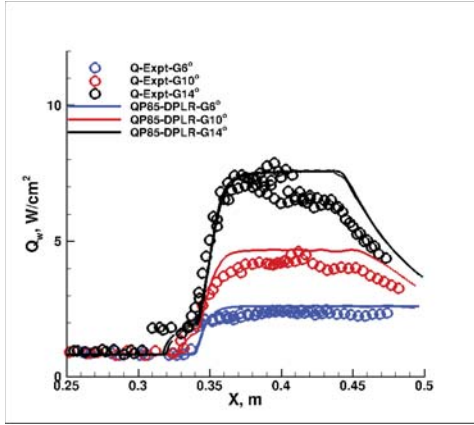


Figure 36. Schülein $M_\infty = 5$ Impinging SWTBL Interaction Wall Heat Transfer Distribution, DPLR/SST QP85 vs Q_{wall} Experimental Measurements: 6° , 10° and 14° Shock Generator Cases.

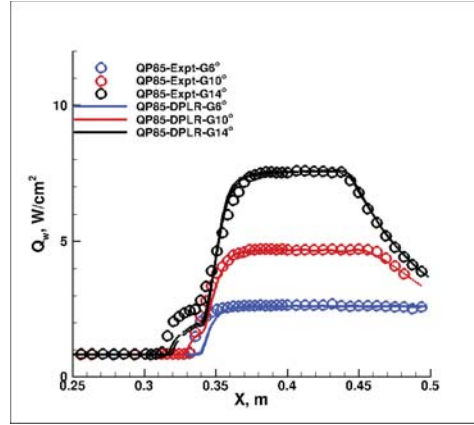


Figure 37. Schülein $M_\infty = 5$ Impinging SWTBL Interaction Wall Heat Transfer Distribution from QP85 Correlation, DPLR/SST vs Expt.: 6° , 10° and 14° Shock Generator Cases.

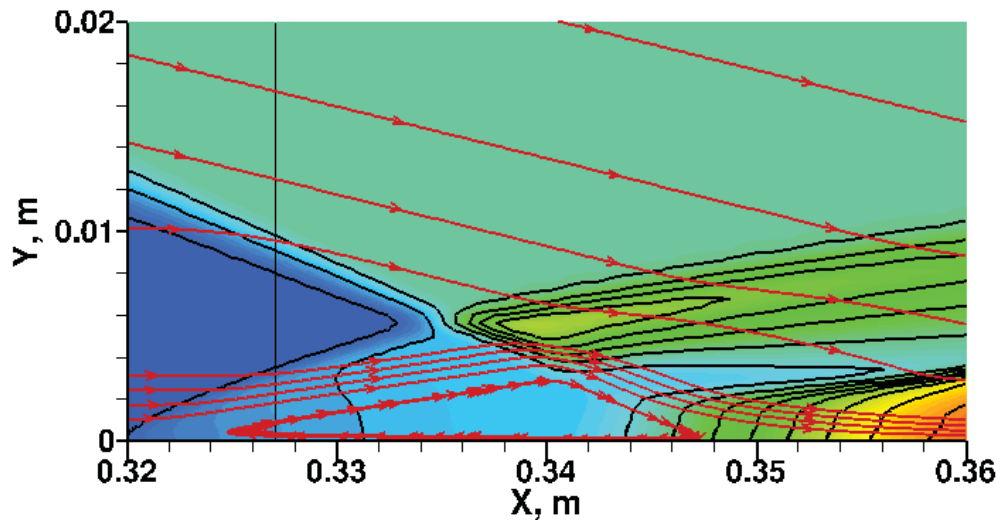


Figure 38. Schülein $M_\infty = 5$ Impinging SWTBL Interaction: Pressure Contours DPLR/SST 14° Shock Generator Case.

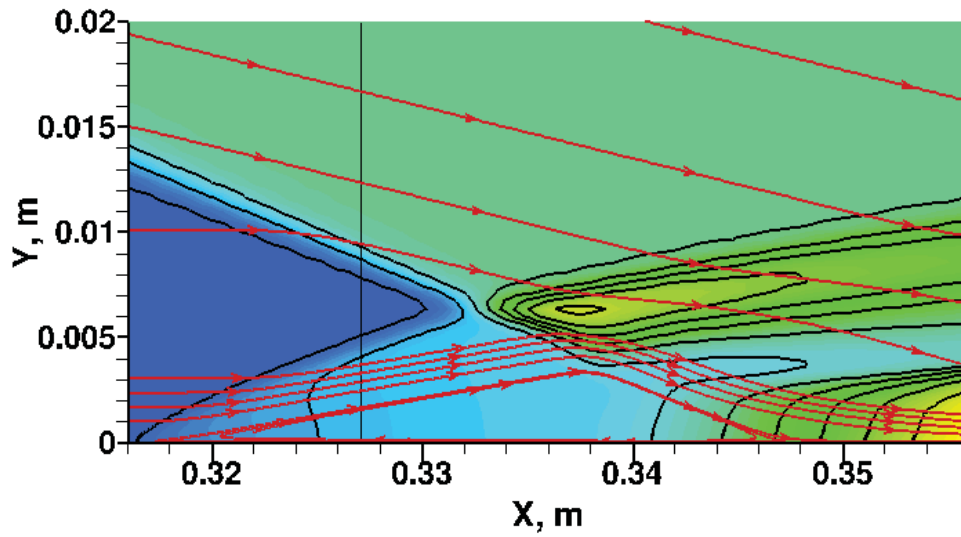


Figure 39. Schülein $M_\infty = 5$ Impinging SWTBL Interaction: Pressure Contours Cf3d/SST 14° Shock Generator Case.

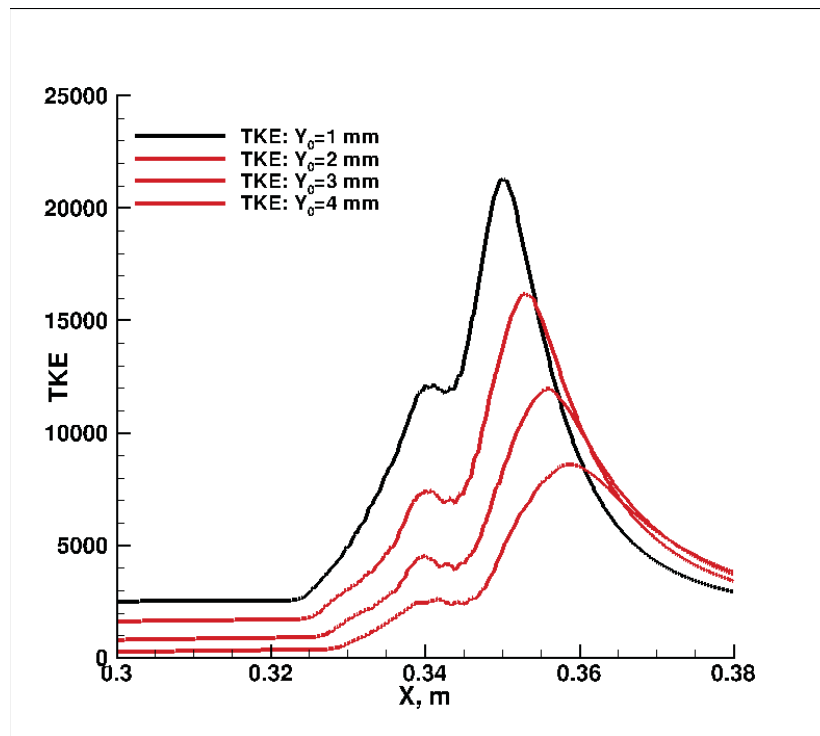


Figure 40. Schülein $M_\infty = 5$ Impinging SWTBL Interaction, 14° case: Development of DPLR/SST Turbulent Kinetic Energy along Boundary Layer Streamlines through the Separation and Reattachment regions.

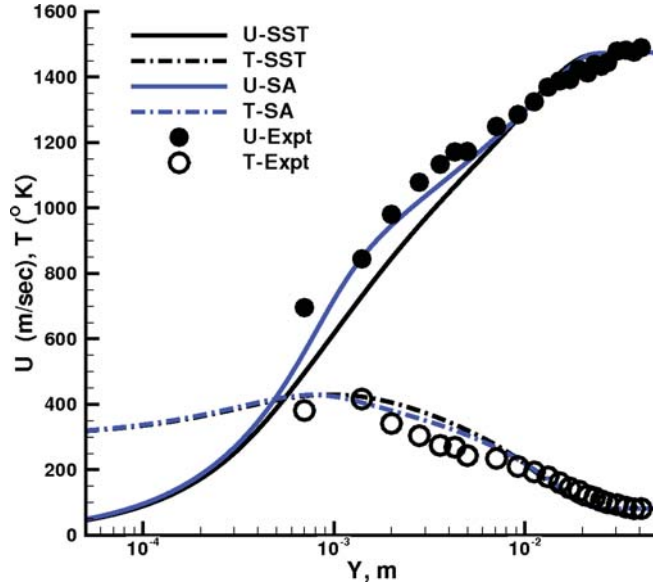


Figure 41. Kussoy $M_\infty = 8.2$ Impinging SWTBL Interaction: Upstream Boundary Layer Velocity and Temperature Profiles: DPLR/SST compared to Experiment.

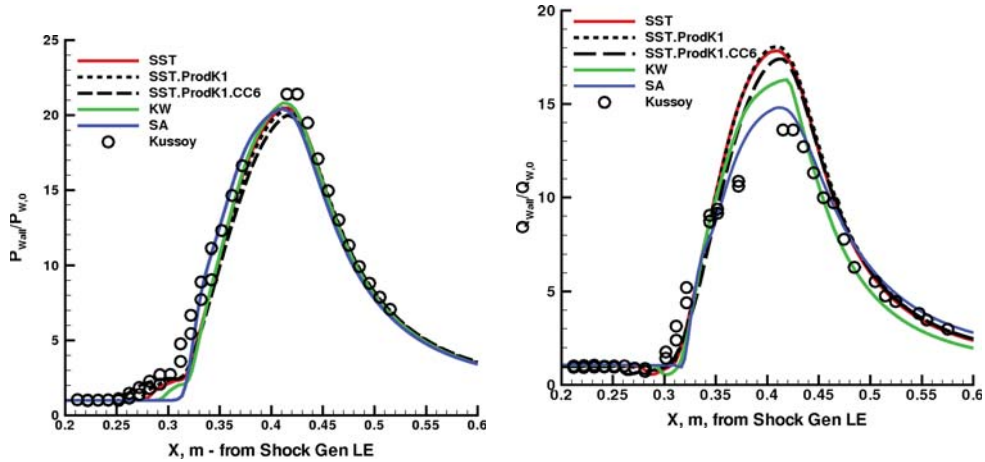


Figure 42. Kussoy $M_\infty = 8.2$ Impinging SWTBL Interaction: Wall Pressure Distribution for DPLR vs Expt, 10° Shock Generator.

Figure 43. Kussoy $M_\infty = 8.2$ Impinging SWTBL Interaction: Wall Heat Transfer Distribution for DPLR vs Expt, 10° Shock Generator.

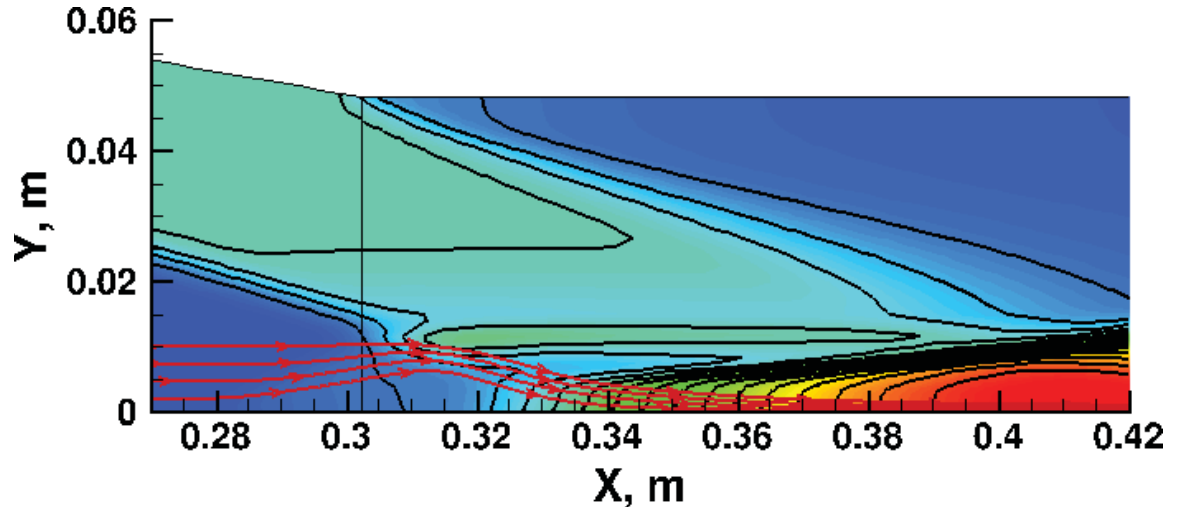


Figure 44. Kussoy $M_\infty = 8.2$ Impinging SWTBL Interaction: Pressure Contours and Contour lines for DPLR/SST, 10° Shock Generator, Expanded Scale.

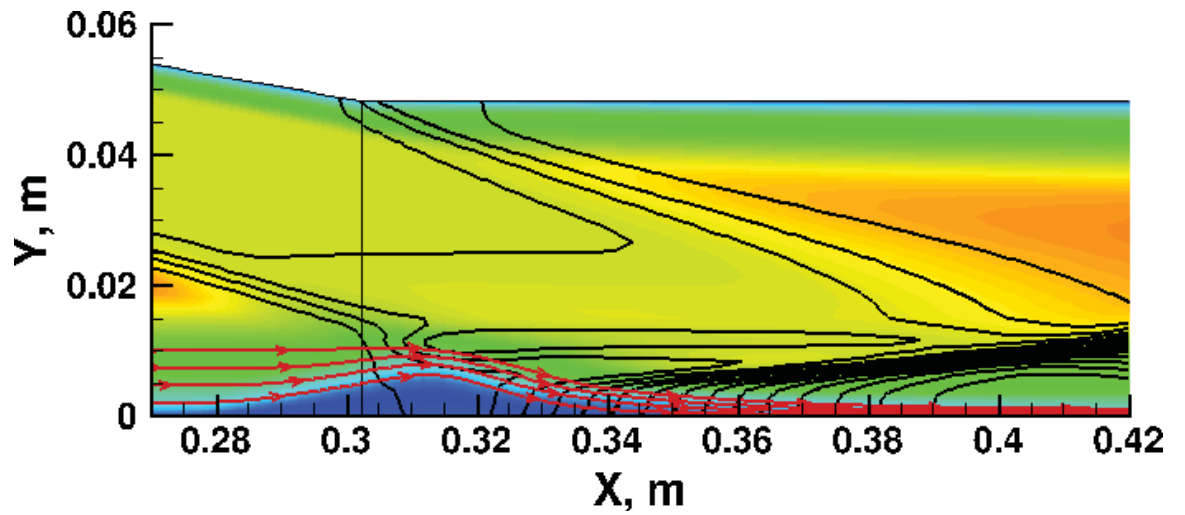


Figure 45. Kussoy $M_\infty = 8.2$ Impinging SWTBL Interaction: Mach Contours and Pressure Contour lines for DPLR/SST, 10° Shock Generator, Expanded Scale.

REPORT DOCUMENTATION PAGE				Form Approved OMB No. 0704-0188	
<p>The public reporting burden for this collection of information is estimated to average 1 hour per response, including the time for reviewing instructions, searching existing data sources, gathering and maintaining the data needed, and completing and reviewing the collection of information. Send comments regarding this burden estimate or any other aspect of this collection of information, including suggestions for reducing this burden, to Department of Defense, Washington Headquarters Services, Directorate for Information Operations and Reports (0704-0188), 1215 Jefferson Davis Highway, Suite 1204, Arlington, VA 22202-4302. Respondents should be aware that notwithstanding any other provision of law, no person shall be subject to any penalty for failing to comply with a collection of information if it does not display a currently valid OMB control number.</p> <p>PLEASE DO NOT RETURN YOUR FORM TO THE ABOVE ADDRESS.</p>					
1. REPORT DATE (DD-MM-YYYY) 01-05-2014		2. REPORT TYPE Technical Memorandum		3. DATES COVERED (From - To)	
4. TITLE AND SUBTITLE <p style="text-align: center;">On Parametric Sensitivity of Reynolds-Averaged Navier-Stokes SST Turbulence Model: 2D Hypersonic Shock-Wave Boundary-Layer Interactions</p>				5a. CONTRACT NUMBER	
				5b. GRANT NUMBER	
				5c. PROGRAM ELEMENT NUMBER	
				5d. PROJECT NUMBER	
				5e. TASK NUMBER	
6. AUTHOR(S) James L. Brown				5f. WORK UNIT NUMBER	
7. PERFORMING ORGANIZATION NAME(S) AND ADDRESS(ES) NASA Ames Research Center Moffett Field, CA 94035-1000				8. PERFORMING ORGANIZATION REPORT NUMBER L-	
9. SPONSORING/MONITORING AGENCY NAME(S) AND ADDRESS(ES) National Aeronautics and Space Administration Washington, DC 20546-0001				10. SPONSOR/MONITOR'S ACRONYM(S) NASA	
				11. SPONSOR/MONITOR'S REPORT NUMBER(S) NASA/TM-2014-218353	
12. DISTRIBUTION/AVAILABILITY STATEMENT Unclassified-Unlimited Subject Category 64 Availability: NASA CASI (443) 757-5802					
13. SUPPLEMENTARY NOTES An electronic version can be found at http://ntrs.nasa.gov .					
14. ABSTRACT Examined is sensitivity of separation extent, wall pressure and heating to variation of primary input flow parameters, such as Mach and Reynolds numbers and shock strength, for 2D and Axisymmetric Hypersonic Shock Wave Turbulent Boundary Layer interactions obtained by Navier-Stokes methods using the SST turbulence model. Baseline parametric sensitivity response is provided in part by comparison with vetted experiments, and in part through updated correlations based on free interaction theory concepts. A recent database compilation of hypersonic 2D shock-wave/turbulent boundary layer experiments extensively used in a prior related uncertainty analysis provides the foundation for this updated correlation approach, as well as for more conventional validation. The primary CFD method for this work is DPLR, one of NASA's real-gas aerothermodynamic production RANS codes. Comparisons are also made with CFL3D, one of NASA's mature perfect-gas RANS codes. Deficiencies in predicted separation response of RANS/SST solutions to parametric variations of test conditions are summarized, along with recommendations as to future turbulence approach.					
15. SUBJECT TERMS Hypersonic, Shock Wave, Turbulent, Boundary Layer					
16. SECURITY CLASSIFICATION OF:			17. LIMITATION OF ABSTRACT	18. NUMBER OF PAGES	19a. NAME OF RESPONSIBLE PERSON
a. REPORT	b. ABSTRACT	c. THIS PAGE			STI Help Desk (email: help@sti.nasa.gov)
U	U	U	UU	68	19b. TELEPHONE NUMBER (Include area code) (443) 757-5802

